

MSc Thesis

A micromechanical model for fault rock friction and the role played by shear bands in determining macroscale behaviour

Martijn van den Ende

Supervised by:

Prof. Dr. C.J. Spiers

Dr. C.J. Peach

Department of Earth Sciences
Utrecht University

October 2013

Student no. 3349373
45 ECTS

Abstract

Gouge-bearing fault rocks often develop characteristic (micro)structural features, such as R₁-, P- and Y micro-shears. In spite of the quite different PT-conditions under which fault rocks may develop, these shear band microstructures are often very similar and show characteristic orientations with respect to the macro-scale sense of shear. This has been widely observed and well described in both experimentally- and naturally produced fault rocks. However, no microphysical model has been developed which explains both the macroscopic rheology and why the observed shear bands are produced. In this thesis, a model is proposed for fault rock friction and the role played by micro-scale shear bands in determining macro-scale behaviour. The approach adopted is as follows. To simulate the initial σ - ε response and shear localising behaviour of a model shear zone, prior to macroscopic yield, it is assumed shear stress increases linearly with shear strain. After a certain amount of strain has been accommodated, the stress state reaches a point at which the system fails in a Mohr-Coulomb fashion producing the first shear band set. The next shear band set is then assumed to form at the orientation that is most favourable for on-going deformation, i.e. the orientation that leads to the lowest macroscopic shear strength. In order to assess what orientation is preferred, the entropy production function is used to identify the lowest entropy production rate. This gives a set of equations where quantities such as the normal stress, the system's cohesive strength, and various frictional parameters can be varied to match experimental observations. In this way, different hypotheses about what causes particular shear band orientations to form, and in what sequence, were systematically tested. The model predicts a range of shear band orientations that falls within the range of orientations observed in both experimentally simulated and in natural fault zones, although comparison with specific experiments reveals that different frictional parameters for the R- versus P-shears are required to reproduce specific orientations seen in such experiments. Moreover, if it is assumed that the R- and P-shears can have different frictional parameters, the macroscopic rheological properties such as the peak stress and steady-state stress observed in specific experiments can be reproduced. The model also predicts that the R-shears activate before the P-shears, which is the order of shear band activation that is typically obtained in experiments. After activation, both these shear bands will then follow an antithetic rotation with respect to the imposed vorticity. This implies that Y-shears can form as a result of R-shear rotation, whereas boundary shears can form by local dilatation at the shear zone boundaries as a result of shear band activity. Even in the current stage of this presented model, valuable insights can be gained regarding the underlying mechanisms for shear band formation and strain accommodation: 1) After the R-shears have formed by Mohr-Coulomb failure, the P-shears form in the orientation that results in the lowest macroscopic shear strength; 2) After shear band formation, isovolumetric strain accommodation results in rotation of both shear bands; 3) Y-shears and boundary shears can form as a result of strain accommodation on the R- and P-shears;

Contents

Abstract	1
1 Introduction.....	3
1.1 Terminology.....	3
1.2 Critical observations in the literature.....	5
2 Symbols and notation.....	9
3 Model geometry and set-up.....	10
4 Background concepts and equations	11
4.1 The entropy production function	11
4.2 The stress/strain state in a material undergoing frictional sliding on two slip planes.....	13
5 Building the model	16
5.1 Matrix anisotropy as a function of shear strain	16
5.2 The activation of R- and P-shears as a result of matrix anisotropy.....	20
5.3 The formation of boundary shears as a result of activity on R- and P-shears.....	25
5.4 The rotation of shear bands as a result of strain.....	27
5.5 The formation of Y-shears as a result of rotation of R- and P-shears	30
6 Model results and discussion	31
6.1 The effect of anisotropy on the order of activation and orientations of R- and P-shears	31
6.2 The effect of anisotropy on the shear strain required for activating R- and P-shears.....	37
6.3 The effect of anisotropy on the initial coefficients of friction of activated R- and P-shears: effects and consequences	38
6.4 The rotation of shear bands and the orientation of σ_1	39
6.5 The effect of an anisotropic starting material.....	42
7 Conclusions and Recommendations for future work.....	43
Acknowledgement.....	45
References.....	45

1 Introduction

It is very common for frictional fault zones to contain weakly cohesive fine-grained rock material, known as (fault) gouge. Most of the strain imposed on an active shear zone is accommodated in this zone containing the gouge. Gouge-bearing fault rocks often develop characteristic (micro)structural features, such as Riedel-, P-, and Y micro-shears (shear bands) that allow for accommodation of the imposed shear strain by frictional sliding on the shear bands' slip surfaces (Logan et al., 1979; Logan, 2007;). In spite of the wide range of PT-conditions at which frictional shear zones develop in nature and experiments, their microstructures are often quite similar and the shear bands show characteristic orientations with respect to the macro-scale sense of shear. This has been widely observed and well described in both experimentally- and naturally produced fault rocks (e.g. Riedel, 1929; Byerlee et al., 1978; Logan et al., 1979; Logan & Rauenzahn, 1987; Power & Tullis, 1989; Keller et al., 1997; Haines et al., 2013). However, despite several qualitative attempts to explain the observations (Tchalenko & Ambraseys, 1970; Haines et al., 2013), no microphysical model has been developed which explains both the macroscopic frictional behaviour of fault gouge and why the observed shear bands are produced. In this thesis, a model is proposed to account for fault rock rheology and the role played by micro-scale shear band properties and geometries in determining macro-scale behaviour.

1.1 Terminology

The terminology used in this thesis is very similar to that of Logan et al. (1979), though minor modifications are applied. The R1- and R2-shears, also known as Riedel shears after Riedel (1929), will in this thesis be referred to as simply R-shears. An R-shear is defined by a fracture making an acute angle with the top block direction of motion. A P-shear is defined by an alignment of mineral grains over which shear displacement is accommodated, and makes an obtuse angle with the top block direction of motion. Y-shears and boundary shears (B-shears) lie parallel or sub-parallel to the shear zone boundaries, where the Y-shears are situated inside the gouge and B-shears at the boundary between the gouge and the shear zone wall or country rock. The terminology for the different shear bands is summarised in Figure (1).

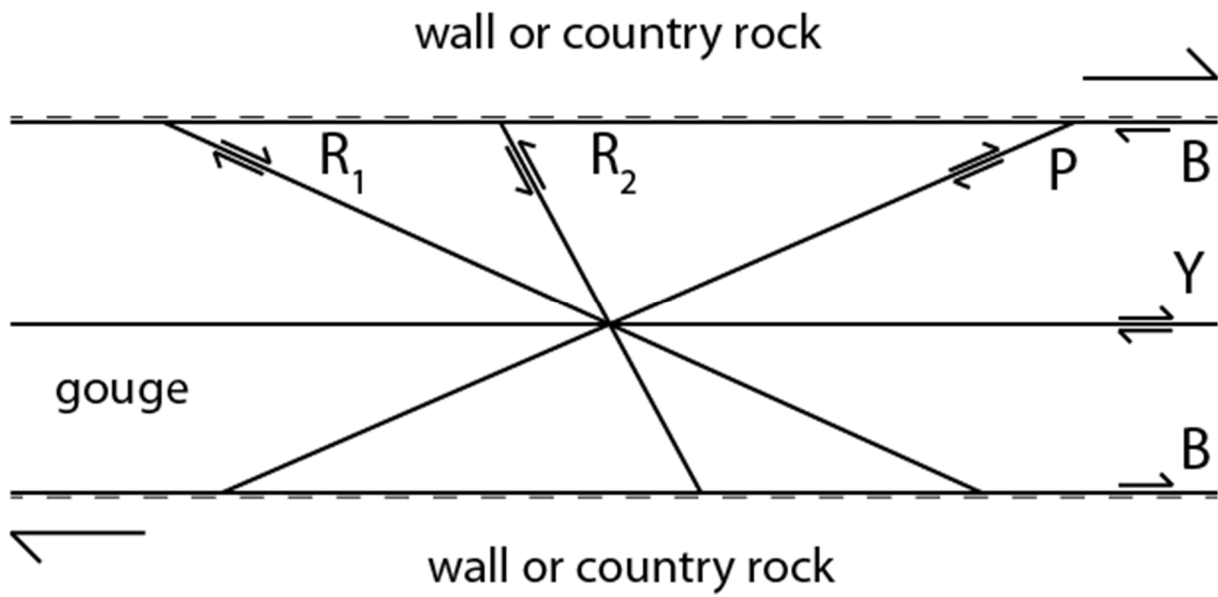


Figure 1: Schematic diagram of the various shear bands typically observed in a gouge-bearing shear zone in nature and experiments. (Note that the orientations are not to scale). After Logan et al. (1979).

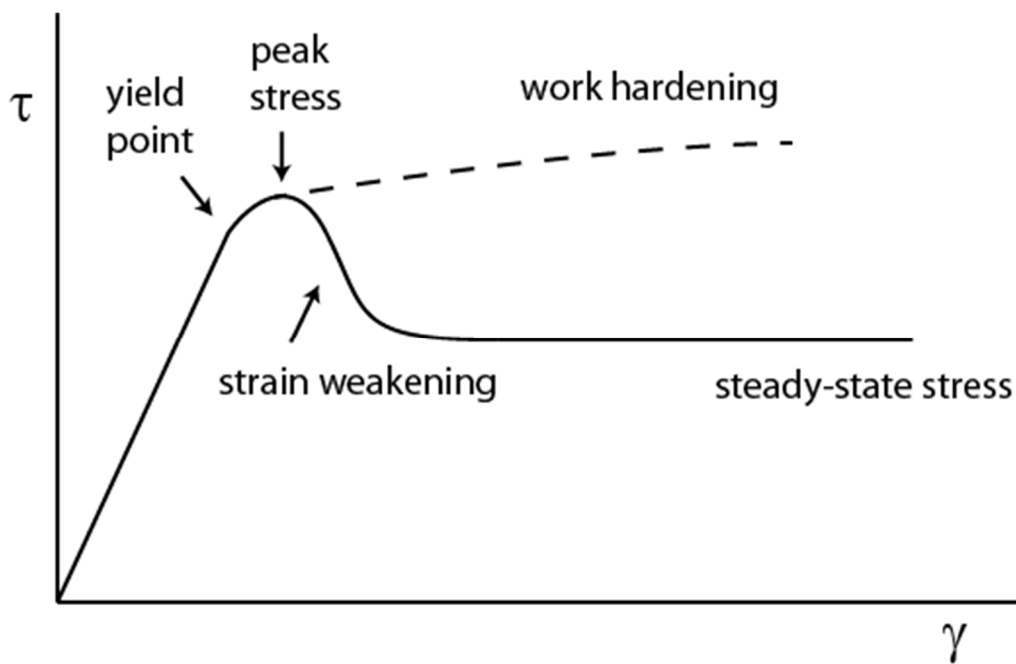


Figure 2: A schematic diagram of the evolution of shear stress with strain in a typical simple shear deformation experiment. See text for clarification

Fig. (2) illustrates the evolution of the shear stress (τ) with shear strain (γ) in a typical simple shear deformation experiment in which a fixed shear displacement rate is imposed at the shear zone boundaries. After an initial near-linear stress build-up, the material starts to yield. In many materials, the stress falls after reaching a peak value soon after yield strain weakening. For higher strains, the measured stress usually stabilises to a steady-state strength value, also called the residual strength, at which the material accommodates slip at a constant strain rate at a fixed shear stress. Some experimental fault zones can also display work hardening, meaning that the stress increases further after the yield point.

1.2 Critical observations in the literature

Fault gouges can be derived from various sources, e.g. sand-, clay- or carbonate rich rocks, and therefore this thesis aims to develop a model that is not restricted to a certain gouge composition, i.e. the model should be capable of predicting fault zone properties of any gouge composition. However, clay rich gouges have been studied most commonly and therefore model development will be based mainly on observations from these studies. Haines et al. (2013) studied the evolution of gouge fabric elements in different clay-rich materials by analysing SEM images from samples that were deformed at different finite shear strains. They describe the following sequence of events that generally is in agreement with the many observations made in experiments conducted on materials other than clay (Logan et al., 1992; Keller et al., 1997; Logan, 2007) and is summarised in Fig. (3):

1. Stress builds linearly with shear strain up to the (apparent) yield point. Typically the yield point is reached at shear strains of $\gamma \approx 1.0$ and has a shear stress between 0.3 and 0.6 times the normal stress, though these values may be higher for materials other than clay, e.g. calcite (Logan et al., 1992) or sandstone (Mandl et al., 1977).
2. For experiments that have been stopped prior to or shortly after the yield point, clay particles are found to form a foliation sub-parallel to the layer margins. This foliation may likely have formed due to normal loading before any shear strain was induced. Other experiments, such as den Hartog et al. (2012), show an initially chaotic foliation that rotates towards the P-orientation with increasing shear strain. Prior to the peak stress, no distinctive fabric elements are formed, but as the peak stress is approached R-shears are reported to nucleate. At the yield point, R-shears are found to be through-going.

3. After the yield point, phyllosilicates were found to be oriented in a P-orientation in the proximity of and between R-shears. Clay particles that lie in regions with no R-shears remained sub-parallel to the shear direction. When a more pervasive network of R-shears has formed, all phyllosilicates lie in a P-orientation.
4. Once formed, the R-shears rotate against the direction of shear (antithetically) towards lower angles with increasing strain. They report as much as 10° rotation over an additional shear strain of about 6. P-shears are not found to rotate, not even for strains up to 20.
5. At the point of stable sliding at a steady-state stress, boundary shears are found to extend along the entire length of the shear zone. At higher strains, Y-shears form where the shallow R-shears rotate into the Y-orientation.

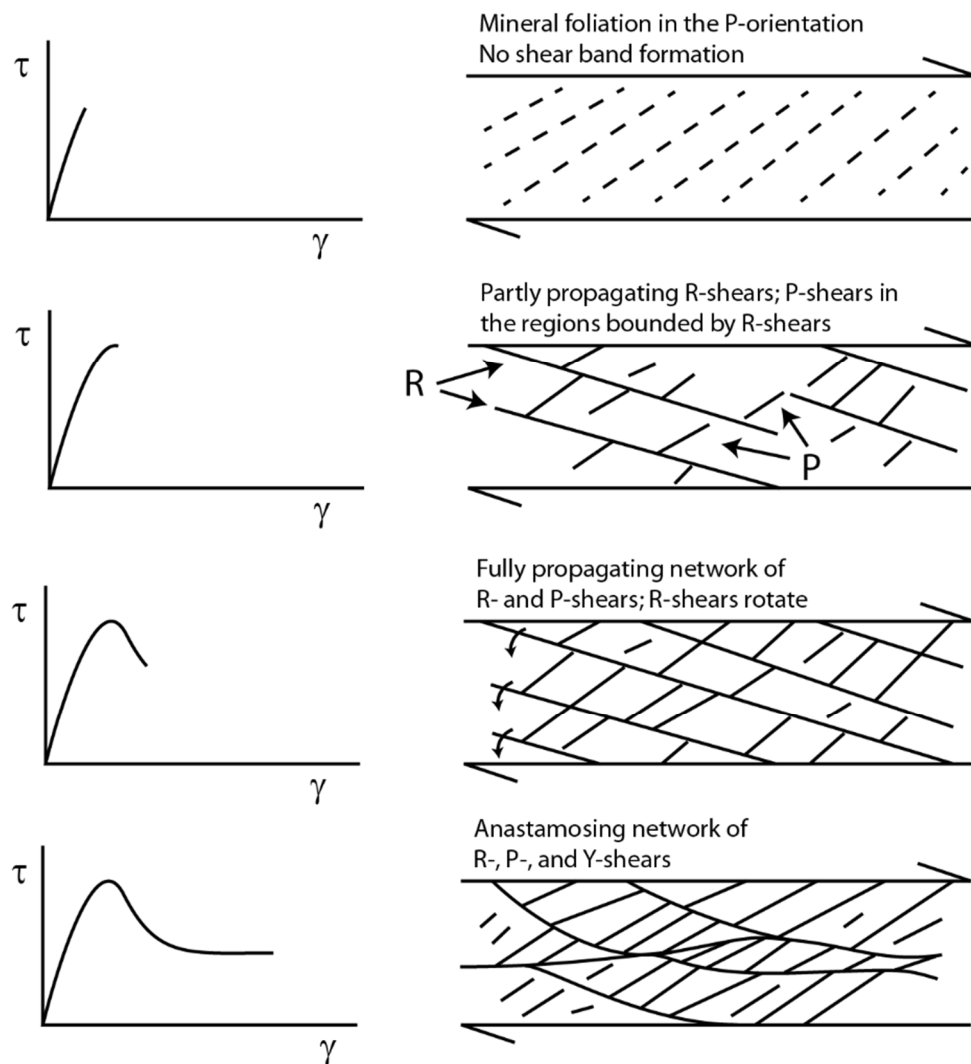


Figure 3: Schematic summary of the evolution of the fault zone fabric with increasing shear strain.

Several experimental studies have demonstrated that in clay-rich gouges R- and P-shears form simultaneously or shortly after (Logan et al., 1979; Keller et al., 1997; Haines et al., 2013), whereas very few or no P-shears form in gouges containing very little or no clay minerals, like sandstone (Byerlee et al., 1978; Logan & Rauenzahn, 1987; Power & Tullis, 1989) or limestone (Logan et al., 1992; Logan, 2007) gouges. In the absence of phyllosilicates, the P-orientation is defined by elongated grains of other minerals that are present that translate and rotate (Hasan & Alshibli, 2012). Also, when phyllosilicates are absent, instead of forming R- and P-shears concurrently, a pervasive network of R-shears forms that curve into a Y-orientation (see Fig. (4)), and Y-shears accommodate the majority of the displacement once they are fully developed (Logan, 2007).

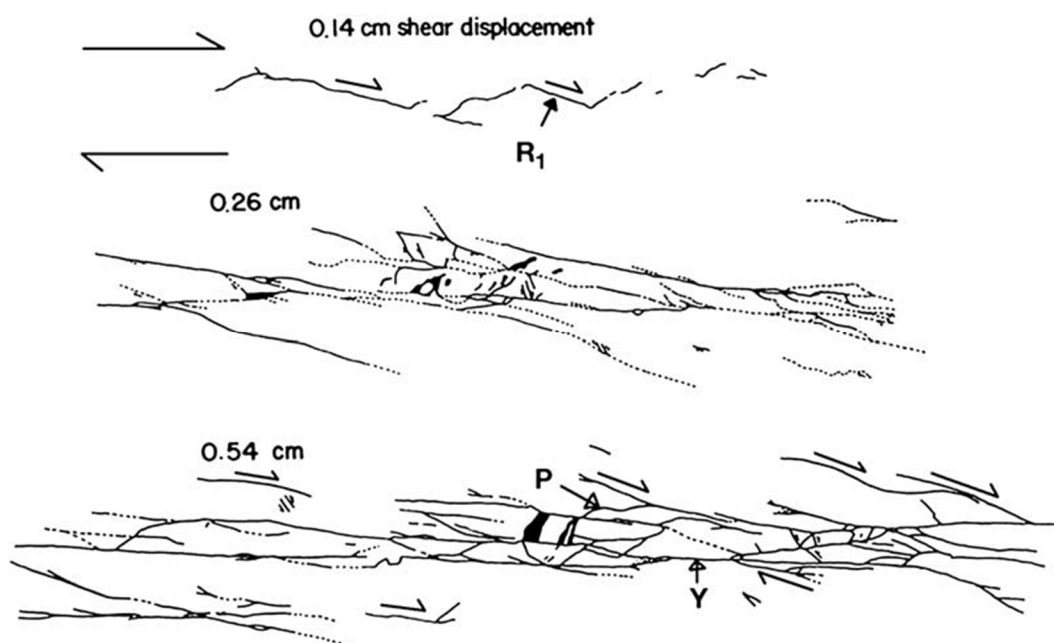


Figure 4: A dextral shear zone map of a 0.5 cm piece of Indiana limestone, deformed at 50 MPa confining pressure for various shear displacements. For the 0.54 cm displacements most of the R-shears have curved into a Y-orientation. Modified by Logan (2007) from Bartlett et al. (1981)

Some of the materials deformed in the experiments of Haines et al. (2013) display work hardening, whereas other materials display strain weakening. The degree of work hardening tends to increase at higher normal stresses, though no systematic relationship between the various materials is found.

For most materials it is found that R-shears typically form at angles between $10^\circ - 20^\circ$ (w.r.t. the shear zone boundary; Logan et al., 1979; Haines et al., 2013). This agrees well with the angles predicted by the Mohr-Coulomb failure criterion assuming that the principal stresses are oriented at 45° w.r.t. the shear zone boundary, i.e. assuming an isotropic material response. If the material were anisotropic, i.e. the strength of the fault zone is directionally dependent, different failure

orientations could be produced (Pietruszczak & Mroz, 2000; Pietruszczak & Mroz, 2001). The orientation of P-shears varies much more from material to material, e.g.: 20° – 35° for crushed chlorite schist (Haines et al., 2013), 10° – 33° for montmorillonite (Haines et al., 2009), 15° – 20° for quartz-anhydrite mixtures (Logan et al., 1979), 10° – 15° for kaolinite (Keller et al., 1997), giving the P-orientation a range between 10° and 35° (Fig. 1). Several studies have suggested that P-shears might orient themselves perpendicular to orientation of the maximum principle stress σ_1 (Tchalenko & Ambraseys, 1970; Logan et al., 1979; Haines et al., 2013).

2 Symbols and notation

In this thesis the Einstein summation convention will be applied in specifying vector and tensor notations, for example:

$$x_i y_i = \sum_{i=1}^n x_i y_i$$

Some symbols may be used for both scalar and tensor quantities. In the latter case, indices will be added. For instance, the bulk strain (scalar) will be denoted as ε , the strain tensor as ε_{ij} . Both notations have the same units.

The time derivative (i.e. the rate of change) of a quantity x will be denoted by \dot{x} .

Angles are measured positive in a counter-clockwise rotation, starting from zero at the intersection with the positive horizontal axis in accordance with a conventional polar coordinate system (Fig. 5).

This convention will occasionally be violated for the sake of convenience. In such cases, a clear definition of how an angle is measured will be given.

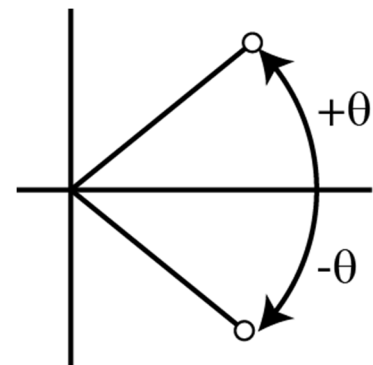


Figure 5: Angles are measured positive in a counter-clockwise rotation, negative in a clockwise rotation.

Table 1 below lists the symbols that are used in this thesis:

SYMBOL	MEANING	UNIT	SYMBOL	MEANING	UNIT
u	Internal energy	$J m^{-3}$	σ	Bulk stress	Pa
w	Work	$J m^{-3}$	σ_n	Normal stress	Pa
q	Heat flow	$J m^{-3}$	τ	Shear stress	Pa
T	Absolute temperature	K	ε	Bulk strain	—
s	Entropy	$J K^{-1} m^{-3}$	γ	Shear strain	—
ζ	Entropy production rate	$J K^{-1} m^{-3} s^{-1}$	ω	Bulk rotation	—
f	Helmholtz free energy	$J m^{-3}$	c	Apparent stiffness coefficient	Pa
n	Plane normal	—	μ	Friction coefficient	—
l	Slip direction	—	μ^0, μ'	Friction parameters	—
α	R-shear angle	$^\circ$	C	Cohesive strength	Pa
β	P-shear angle	$^\circ$	S	Sum of shear band activity	—
J	Total deformation	—	$\hat{\gamma}$	Relative activation strain	—

Table 1: A list of the symbols used in this thesis with explanation and units.

3 Model geometry and set-up

The shear zone gouge layer is modelled as a zone of finite but undefined thickness into the vertical x_2 -direction, stretching to infinity in the horizontal x_1 -direction. The country rock outside this layer is rigid (infinitely stiff), but the shear zone material itself is assumed to obey a linear $\tau - \gamma$ relationship to allow permanent strain. The shear direction is dextral (top block to the right). The normal vector n_i and the slip direction vector l_i of the R- and P-shears are defined by their angles α and β respectively. These angles are measured positively counter-clockwise relative to the shear zone boundary, where $90^\circ < \alpha \leq 180^\circ$ and $0 < \beta \leq 90^\circ$. The geometry of the model is summarised in Figure (5).

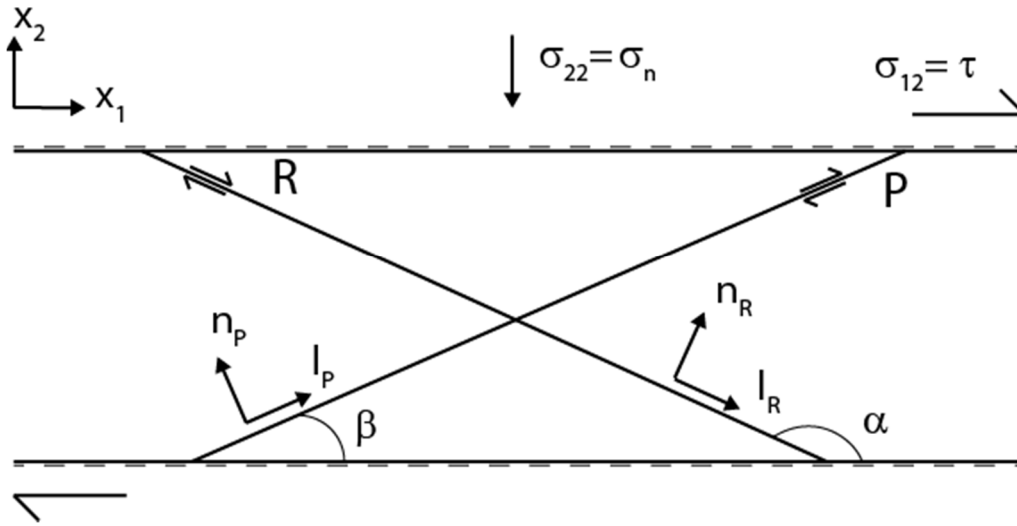


Figure 6: The basic model geometry. The orientation n_i and slip direction l_i of R and P are defined by their angles α and β respectively, measured positively counter-clockwise relative to the shear zone boundary.

It is assumed that densely distributed arrays, i.e. an infinite number of R- and P-shears are present once they have formed. From the geometry, it follows that the R-shear normal and slip direction, n_R and l_R are given by the unit vectors or direction cosines of Fig. (6):

$$n_R = \begin{bmatrix} \sin(\alpha) \\ -\cos(\alpha) \end{bmatrix}, \quad l_R = \begin{bmatrix} -\cos(\alpha) \\ -\sin(\alpha) \end{bmatrix} \quad (1)$$

Similarly for the P-shears:

$$n_P = \begin{bmatrix} -\sin(\beta) \\ \cos(\beta) \end{bmatrix}, \quad l_P = \begin{bmatrix} \cos(\beta) \\ \sin(\beta) \end{bmatrix} \quad (2)$$

4 Background concepts and equations

4.1 The entropy production function

The first law of thermodynamics states that energy is always conserved. For a stationary body, it is written:

$$du = w + q \quad (3)$$

where u is the internal energy, w the work added to the system, and q the heat flow into the system. The second law of thermodynamics states that the total entropy can never decrease:

$$Tds - dq \geq 0 \quad (4)$$

where T is the absolute temperature, and s the total entropy. For a reversible process and for a system in equilibrium, (4) equates to zero. A system that deforms inelastically or permanently is not in equilibrium, and therefore it is useful to define a quantity ζ as follows:

$$T\zeta \equiv T\dot{s} - \dot{q} \quad (5)$$

Where \dot{s} and \dot{q} are the rate of change of the total entropy and the system's heat flow respectively. ζ is the rate of entropy production within the system and measures how far the system is from the equilibrium situation, where $\zeta = 0$ (de Groot & Mazur, 1984).

The Helmholtz free energy f is defined as:

$$f \equiv u - Ts \quad (6)$$

And its time-derivatives as:

$$\dot{f} = \dot{u} - T\dot{s} \quad (7)$$

Since u and s are universally valid state variables, f is universal and can thus be applied to non-hydrostatic systems, as opposed to the commonly used Gibbs free energy, which is formally defined only for hydrostatic systems (Lehner & Bataille, 1984). Substituting (5) in (7) gives:

$$\dot{f} = \dot{u} - \dot{q} - T\zeta \quad (8)$$

Then (3) can be substituted in (8) to give:

$$\dot{f} = \dot{w} - T\zeta \quad (9)$$

A system in true (microstructural) steady-state, though not necessarily in equilibrium, has $\dot{f} = 0$ (as there is no change in thermodynamic state). This gives:

$$T\zeta = \dot{w} \quad (10)$$

The work rate done by or onto a system is often defined as force times velocity, but it can be defined more generally as:

$$\dot{w} = \sigma_{ij} \frac{\partial \varepsilon_{ij}}{\partial t} + \frac{1}{2} \frac{\partial \sigma_{ij}}{\partial t} \frac{\partial \varepsilon_{ij}}{\partial t} \approx \sigma_{ij} \dot{\varepsilon}_{ij} \quad (11)$$

where σ_{ij} and ε_{ij} are the stress and strain tensors respectively. This simplifies (10) to:

$$T\zeta = \sigma_{ij} \dot{\varepsilon}_{ij} \quad (12)$$

Note here that all intensive energy quantities or derivations are expressed per unit material volume in the current state and not in a pre-defined reference state. This means we can use the Cauchy stress and conventional strain tensor as opposed to the Piola-Kirchhoff stress and conjugate strain tensor (Chaves, 2013). This choice is justified for a system at constant mass and constant σ_{ij} or for an incompressible material. In a two-dimensional simple shear deformation $\dot{\varepsilon}_{ij} = \frac{1}{2} \begin{bmatrix} 0 & \dot{\gamma} \\ \dot{\gamma} & 0 \end{bmatrix}$, $\sigma_{ij} \dot{\varepsilon}_{ij}$

simplifies to $\tau \dot{\gamma}$ and (12) simplifies further to:

$$T\zeta = \tau \dot{\gamma} \quad (13)$$

where τ and $\dot{\gamma}$ are the shear stress and shear strain rate respectively.

In the Taylor formulation of the Taylor-Bishop-Hill model, the combination of slip systems is chosen that results in the lowest work done accommodating the imposed strain, provided that the chosen combination is geometrically capable of accommodating the imposed displacement. In other words,

given the critical shear stress τ_k of each k -th slip system, the set of $\dot{\gamma}_k$ is chosen to minimise $\dot{w} = \tau_k \dot{\gamma}_k$, where $\dot{\gamma}_k$ is given by $\frac{1}{2}(l_i n_j + l_j n_i)_k \dot{\gamma}_k = \dot{\epsilon}_{ij}$ (Taylor, 1938; Lister et al., 1978). Following this principle, the set of shear bands in the model fault zone is chosen so that (13) is minimised. If $\dot{\gamma}$ is assumed constant, minimising of (13) results in a minimum τ . In other words, the energetically most favourable configuration of the system will be the one that leads to the lowest shear stress required to shear the system at a constant strain rate.

4.2 The stress/strain state in a material undergoing frictional sliding on two slip planes

This problem is treated here in a similar manner as the approach originally applied by Taylor (1938) for analysing crystal plastic deformation of single crystals, which was later reformulated by Bishop & Hill (1951). In the Taylor-Bishop-Hill model for crystal plastic deformation, it is assumed that a certain external strain imposed on a single crystal is accommodated by slip on several slip systems that operate within the crystal lattice. Von Mises (1928) derived that, in a two-dimensional system, there are two slip systems required to accommodate any general strain for the constraint that deformation does not produce any volumetric strain, i.e. $\epsilon_{ii} = 0$. This was done by considering the independent components of a general strain tensor ϵ_{ij} . By definition, ϵ_{ij} is symmetrical and has therefore three independent components. By requiring that $\epsilon_{ii} = 0$ (implying $\epsilon_{11} = -\epsilon_{22}$), only two independent components remain, which can be satisfied by two independent slip systems (two variables solved by two equations).

A fault zone that accommodates strain by isovolumetric slip on shear band can be treated similarly as the Taylor-Bishop-Hill approach for single crystals. Just like a crystal, the fault zone would require two independent slip systems (the R- and P-shears) to accommodate any general non-volumetric strain. Analogously to the activation of slip systems in a crystal, shear bands are activated when the shear stress acting on the slip plane reaches the critical resolved shear stress of that plane. The shear stress acting on the k -th shear band is given by (Lister et al., 1978):

$$\tau_k = \frac{1}{2}(l_i n_j + l_j n_i)_k \sigma_{ij} \quad (14)$$

Here l_i is the top block shear direction, and n_i the normal of the shear band (see Fig. 5). At the same time, in order to activate the shear band (i.e. to have slip), the Mohr-Coulomb failure criterion must be satisfied:

$$\tau_k = \mu_k(\sigma_n)_k = \mu_k \sigma_{ij}(n_i n_j)_k \quad (15)$$

Equation (14) must equal (15), which gives:

$$\frac{1}{2}(l_i n_j + l_j n_i)_k \sigma_{ij} = \mu_k \sigma_{ij}(n_i n_j)_k \quad (16)$$

Equation (16) has 3 unknowns (3 independent components of σ_{ij}) and since there are two shear bands that operate simultaneously, it yields 2 independent equations ($k = \{1,2\}$, one for the R-shears, one for the P-shears). Lastly, in order to solve this system of equations for σ_{ij} , we note that $\sigma_{22} = \sigma_n$, which is a necessary requirement for stress equilibrium. Rewriting (16) into a matrix-vector multiplication gives:

$$\begin{bmatrix} (l_1 n_1)_R - \mu_R(n_1^2)_R & (l_1 n_2 + l_2 n_1)_R - 2\mu_R(n_1 n_2)_R & (l_2 n_2)_R - \mu_R(n_2^2)_R \\ (l_1 n_1)_P - \mu_P(n_1^2)_P & (l_1 n_2 + l_2 n_1)_P - 2\mu_P(n_1 n_2)_P & (l_2 n_2)_P - \mu_P(n_2^2)_P \\ 0 & 0 & 1 \end{bmatrix} \begin{bmatrix} \sigma_{11} \\ \sigma_{12} \\ \sigma_{22} \end{bmatrix} = \begin{bmatrix} 0 \\ 0 \\ \sigma_n \end{bmatrix} \quad (17)$$

The matrix in (17) is invertible, so that this system of equations can be solved relatively easily. The resulting σ_{ij} is the state of stress required to have both systems active simultaneously, which in turn is required to further accommodate a general strain. In addition, cohesion can be given to any of the shear bands by changing the right-hand side of (17) into $[C_R \ C_P \ \sigma_n]^T$, with C_R and C_P being the cohesion for the R- and P-shears respectively.

Any position gradient tensor J_{ij} can be split in a symmetrical irrotational strain tensor ε_{ij} and an anti-symmetric rigid body rotation tensor ω_{ij} as follows (Ranalli, 1995):

$$J_{ij} = \frac{1}{2}(J_{ij} + J_{ji}) + \frac{1}{2}(J_{ij} - J_{ji}) = \varepsilon_{ij} + \omega_{ij} \quad (18)$$

For a simple shear type of deformation $J_{ij} = \begin{bmatrix} 0 & \gamma \\ 0 & 0 \end{bmatrix}$, so that:

$$\varepsilon_{ij} = \begin{bmatrix} 0 & \gamma/2 \\ \gamma/2 & 0 \end{bmatrix} \quad (19)$$

Taylor (1938) derived that for a 2-dimensional system, any deformation can be accommodated by allowing slip on two slip planes, in this case the R- and P-shears:

$$J_{ij} = \sum_{k=1}^N (J_{ij})_k = \sum_{k=1}^N (l_i n_i \gamma)_k \quad (20)$$

From (18) it follows that the strain tensor can be written as:

$$\varepsilon_{ij} = \sum_{k=1}^N \frac{1}{2} (l_i n_j + l_j n_i)_k \gamma_k \quad (21)$$

And that the rotation tensor can be written as:

$$\omega_{ij} = \sum_{k=1}^N \frac{1}{2} (l_i n_j - l_j n_i)_k \gamma_k \quad (22)$$

For a known ε_{ij} , γ_k can be solved for quite easily (2 independent components of ε_{ij} , 2 unknowns γ_R and γ_P). Rewriting (21) and substituting (19) into it gives:

$$\begin{bmatrix} (l_1 n_1)_R & (l_1 n_1)_P \\ \frac{1}{2} (l_1 n_2 + l_2 n_1)_R & \frac{1}{2} (l_1 n_2 + l_2 n_1)_P \end{bmatrix} \begin{bmatrix} \gamma_R \\ \gamma_P \end{bmatrix} = \begin{bmatrix} 0 \\ \gamma/2 \end{bmatrix} \quad (23)$$

Where the subscripts R and P denote the R- and P-shears respectively. Substituting (1) and (2) in (23) and solving the system of equations gives:

$$\begin{bmatrix} \gamma_R \\ \gamma_P \end{bmatrix} = \frac{\gamma}{\sin(2\beta - 2\alpha)} \begin{bmatrix} \sin(2\beta) \\ \sin(-2\alpha) \end{bmatrix} \quad (24)$$

Where α and β are the angles of the R- and P-shears respectively w.r.t. the shear zone boundary.

Once R- and P-shears have formed, the system accommodates the imposed strain by slip on those two shear bands, rather than deforming the matrix any further, assuming that frictional sliding on those shear bands results in a lower fault zone strength than deformation of the matrix.

5 Building the model

5.1 Matrix anisotropy as a function of shear strain

When a clay-rich gouge sample is deformed up to the peak strength, a mineral foliation develops quite rapidly. This foliation causes the matrix to become anisotropic, allowing easy slip parallel to the weak clay minerals. It is not unrealistic to assume that, starting with randomly oriented clay particles in the matrix, this matrix foliation forms parallel to the long axis of the strain ellipse (Turner, 1957; Twiss & Moores, 2007). As the matrix accommodates more strain, the strain ellipse rotates and stretches. The ellipse radius would be a good measure for both the orientation and the elongation of the strain ellipse.

The deformation gradient tensor F_{ij} for a simple shear deformation is:

$$F = \begin{bmatrix} 1 & \gamma \\ 0 & 1 \end{bmatrix}$$

The Cauchy strain tensor C_{ij} is defined as:

$$C \equiv F^{-T} F^{-1} = \begin{bmatrix} 1 & -\gamma \\ -\gamma & 1 + \gamma^2 \end{bmatrix} \quad (25)$$

The eigenvalues of C_{ij} represent the *reciprocal quadratic elongations*, and its eigenvectors represent the *principal stretching axes* (Fossen, 2010). By solving for the eigenvectors one can describe the strain ellipse as a function of strain. The eigenvalues are obtained by solving:

$$\det(C - \lambda I) = 0$$

$$\begin{vmatrix} 1 - \lambda & -\gamma \\ -\gamma & 1 + \gamma^2 - \lambda \end{vmatrix} = 0$$

$$(1 - \lambda)(1 + \gamma^2 - \lambda) - \gamma^2 = 0 \quad (26)$$

The general solution for (26) is:

$$\lambda = \frac{1}{2} \left(2 + \gamma^2 \pm \gamma \sqrt{4 + \gamma^2} \right) \quad (27)$$

Note that λ contains both of the two solutions. The eigenvectors are then found by substituting (27) for λ and solving:

$$\begin{bmatrix} 1 - \lambda & -\gamma \\ -\gamma & 1 + \gamma^2 - \lambda \end{bmatrix} \begin{bmatrix} v_1 \\ v_2 \end{bmatrix} = \begin{bmatrix} 0 \\ 0 \end{bmatrix}$$

$$\hat{v}_i = \begin{bmatrix} \gamma \\ 1 - \gamma \end{bmatrix} \frac{1}{\sqrt{\gamma^2 + (1 - \lambda)^2}} \quad (28)$$

Here \hat{v}_i is the normalized eigenvector. Since the eigenvalues represent the *reciprocal quadratic elongations*, the smallest eigenvalue λ_2 corresponds to the length of the long axis of the strain ellipse:

$$\lambda_2 = \frac{1}{2} \left(2 + \gamma^2 - \gamma \sqrt{4 + \gamma^2} \right) \quad (29)$$

Substituting λ_2 in (28) gives the eigenvector \hat{v}_{max} oriented parallel to the long axis. The acute angle between \hat{v}_{max} and the shear zone boundary (horizontal plane) is then given by the dot product of \hat{v}_{max} and the coordinate vector $e^x = [1 \ 0]^T$:

$$\hat{v}_{max} \cdot e^x = \cos(A) = \frac{\gamma}{\sqrt{\gamma^2 + (1 - \lambda_2)^2}} \quad (30)$$

where A is the acute angle between the strain ellipse long axis and the shear zone boundary.

The next thing is to describe the radius of the ellipse as a function of γ . A flat-lying ellipse having its long axis parallel to the x-axis can generally be described as:

$$\frac{x^2}{a} + \frac{y^2}{b} = 1 \quad (31)$$

where a and b are the lengths of the long and short axis respectively. In the case of the strain ellipse, a and b are given by:

$$a = \frac{1}{\sqrt{\lambda_2}}, \quad b = \frac{1}{\sqrt{\lambda_1}} \quad (32)$$

The x and y coordinates at any point on the ellipse can be accordingly described as:

$$\begin{bmatrix} x \\ y \end{bmatrix} = r \begin{bmatrix} \cos(\theta) \\ \sin(\theta) \end{bmatrix} \quad (33)$$

where r is the radius of the ellipse at coordinates (x, y) and θ is the angle between the x-axis and the vector $[x \ y]^T$. Substituting (32) and (33) into (31) now gives:

$$\sqrt{\lambda_2} r^2 \cos^2(\theta) + \sqrt{\lambda_1} r^2 \sin^2(\theta) = 1 \quad (34)$$

Then, solving for r yields:

$$r = (\sqrt{\lambda_2} \cos^2(\theta) + \sqrt{\lambda_1} \sin^2(\theta))^{-1/2} \quad (35)$$

In equation (35) it was assumed that the long axis of the ellipse lies parallel to the x-coordinate. This is of course not correct for the strain ellipse, but equation (30) provides its orientation, thus (35) can be corrected to represent the radius of an ellipse tilted to angle A :

$$r = (\sqrt{\lambda_2} \cos^2(\theta - A) + \sqrt{\lambda_1} \sin^2(\theta - A))^{-1/2} \quad (36)$$

Equation (36) now describes the radius of the strain ellipse as a function of strain ($\lambda, A = f(\gamma)$) and orientation of a plane making an angle θ w.r.t. the x-coordinate. For $\gamma = 0$ (no strain), $\lambda_1 = \lambda_2 = 1$, so that $r = 1$ for any value of θ , i.e. the strain ellipse is a circle with unit radius. For $\gamma \rightarrow \infty$, $\lambda_1 \rightarrow \infty$ and $\lambda_2 \rightarrow 0$. If then a plane is oriented parallel to the long axis of the strain ellipse, i.e. $\theta = A$, then $r \rightarrow \infty$. If a plane lies parallel to the short axis ($\theta - A = 90^\circ$), then $r \rightarrow 0$.

Now r can be used as a measure of the degree of anisotropy caused by the foliation of clay minerals. This is done by building r into an equation for the friction coefficient μ . A reasonable choice for this equation would be:

$$\mu(\gamma, \theta) = \mu^0 \exp(-\mu' [r - 1]) \quad (37)$$

where μ^0 and μ' are coefficients to scale μ to reasonable values. μ^0 determines the initial (isotropic) strength of a material, μ' the sensitivity to anisotropy or the rate at which anisotropy develops.

Linking μ to r in this manner prevents μ from becoming negative like when a linear relationship is used. It is assumed that the same parameters apply throughout the system, giving the R- and P-shears the same friction parameters, but the difference in orientation gives them difference friction coefficients. Initially (before any strain is applied) $\gamma = 0$, $r = 1$ and (37) reduces to:

$$\mu(0, \theta) = \mu^0 \quad (38)$$

This is the isotropic base-case where the material has the same coefficient of friction in any direction. When an infinite amount of strain is applied ($\gamma \rightarrow \infty$), the range that μ can span is limited by two end-members:

$$\mu(\infty, A) = \mu^0 \exp(-\mu'[\infty - 1]) = 0 \quad (39)$$

$$\mu(\infty, A \pm 90^\circ) = \mu^0 \exp(-\mu'[0 - 1]) = \mu^0 \exp(\mu') \quad (40)$$

The choice for an exponential equation in (37) ensures that the μ does not drop below zero and also that μ has an upper limit, although this upper limit can still be extremely high depending on the chosen values of μ^0 and μ' . However, it is expected that in reality these limits will never be reached, since the matrix cannot accommodate an infinite amount of strain before brittle/plastic failure occurs. An example of how μ evolves with strain that is accommodated by the matrix is shown in Figure (7).

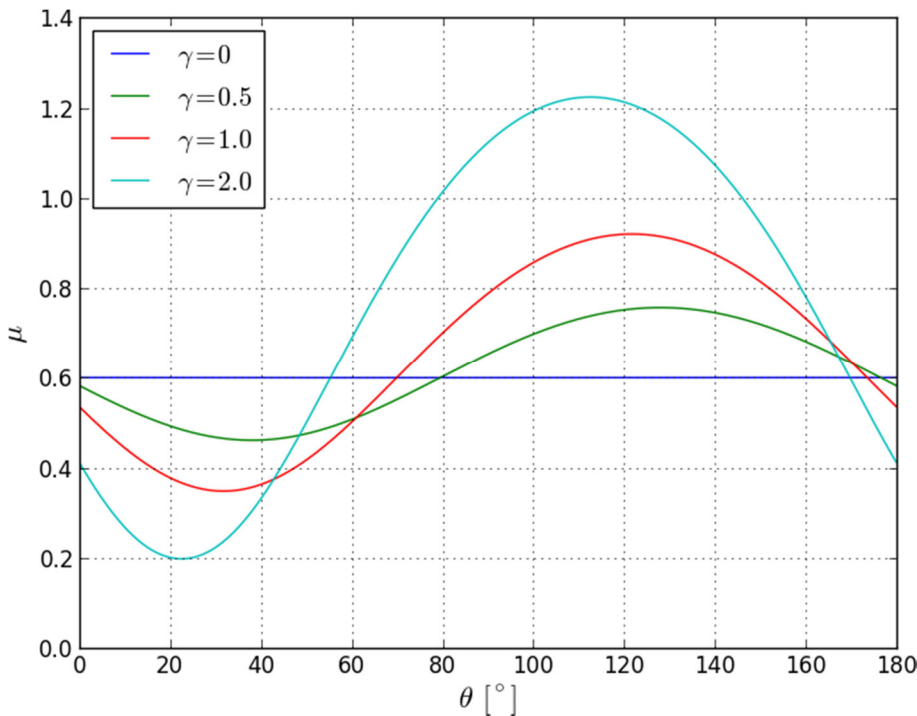


Figure 7: The value of the friction coefficient μ as a function of orientation θ for various amounts of shear strain γ . For $\gamma = 0$, μ is independent of orientation, making the material isotropic. In this example, values for μ^0 and μ' are assumed 0.6 and 2.0 respectively.

5.2 The activation of R- and P-shears as a result of matrix anisotropy

When a material is isotropic, it is assumed to fail at a stress state dictated by an isotropic (i.e. with orientation independent parameters) Mohr-Coulomb failure criterion:

$$|\tau_k| = \mu_k(\sigma_n)_k + C \quad (41)$$

The orientation of the failure plane will follow from:

$$2\varphi = 90^\circ - \text{atan}(\mu) \quad (42)$$

$$2\theta = 90^\circ + \text{atan}(\mu) \quad (43)$$

where φ is the angle between the failure plane and the maximum principal stress (σ_1) orientation and θ is the angle between the failure plane normal and σ_1 . For a state of stress that would result in a simple shear type of strain (in an isotropic material), σ_1 is oriented at 135° to the shear zone boundary. The orientation of the failure plane w.r.t. the shear zone boundary can thus be expressed as:

$$\alpha = 135^\circ + \varphi = 180^\circ - \frac{1}{2}\text{atan}(\mu) \quad (44)$$

For an isotropic material with a coefficient of friction of 0.6, the angle between the failure plane and the shear zone boundary would be approximately 165° (ignoring conjugate orientations).

When a linear stress-strain relationship is assumed in the loading stage prior to formation R- and P-shears, i.e. when $\tau = c\gamma$ (where c is a constant), with a confining normal stress σ_n , the state of stress is:

$$\sigma_{ij} = \begin{bmatrix} \sigma_n & c\gamma \\ c\gamma & \sigma_n \end{bmatrix} = \begin{bmatrix} 0 & c\gamma \\ c\gamma & 0 \end{bmatrix} + I\sigma_n \quad (45)$$

The principal stresses defining the position of the Mohr circle then follow from the eigenvalues of (45) and given by:

$$\lambda = \sigma_n \pm c\gamma \quad (46)$$

The state of stress of any point on the Mohr circle would then be:

$$\tau_k = \frac{1}{2}(\sigma_1 - \sigma_2) \sin 2\theta = c\gamma \sin 2\theta \quad (47)$$

$$(\sigma_n)_k = \frac{1}{2}(\sigma_1 + \sigma_2) + \frac{1}{2}(\sigma_1 - \sigma_2) \cos 2\theta = \sigma_n + c\gamma \cos 2\theta \quad (48)$$

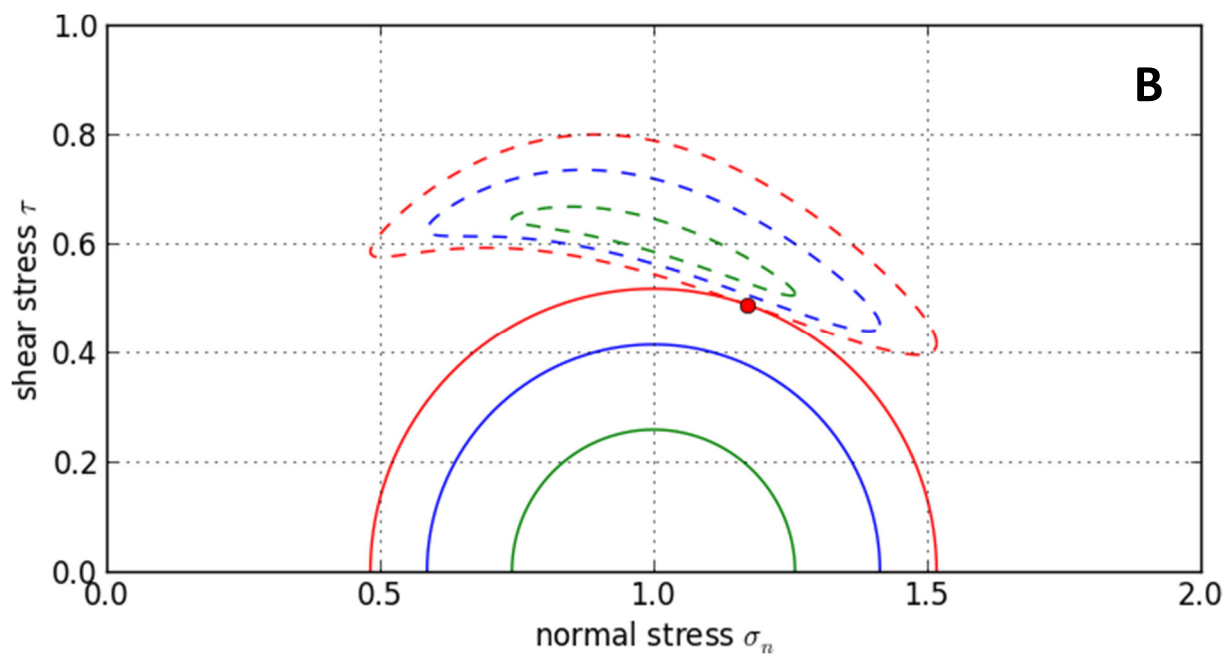
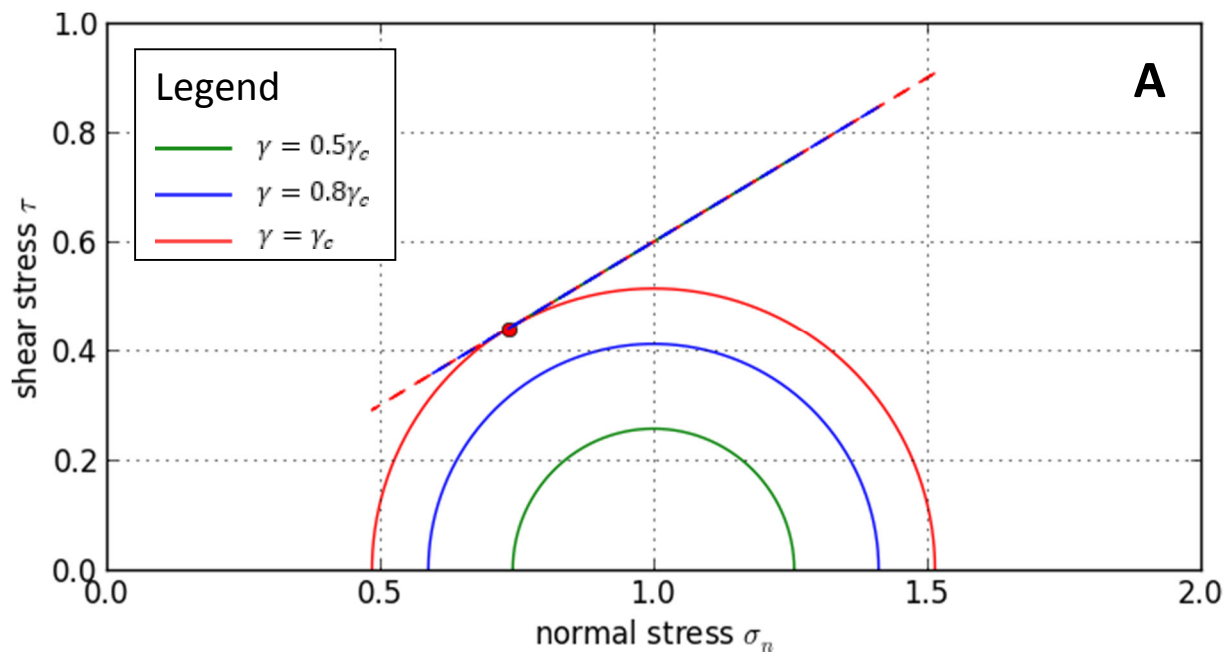
For an anisotropic system, the failure envelope is directionally dependent. The envelope is given here by:

$$\mu_k(\sigma_n)_k + C = \mu_k(\sigma_n + c\gamma \cos 2\theta) + C \quad (49)$$

Note that μ_k is directionally dependent as well for $\mu' > 0$. Equation (49) can then be solved for $0 \leq |2\theta| \leq 180^\circ$ to render the anisotropic envelopes as seen in Fig. (8). In Fig. (8A), where the system is isotropic ($\mu' = 0$), the envelopes are represented by straight lines. In Fig. (8) and (8C) the system is anisotropic ($\mu' > 0$) and the envelopes start to curve and rotate with increasing matrix anisotropy. The envelope represents the frictional resistance to slip at any given orientation and failure occurs when the envelope hits the Mohr-circle, i.e. when (41) is satisfied, or $|\tau_k| - \mu_k(\sigma_n)_k - C = 0$. Substituting (47) and (48) in (41) now gives:

$$|c\gamma \sin 2\theta| - \mu_k(\sigma_n + c\gamma \cos 2\theta) - C = 0 \quad (50)$$

This equation cannot be solved analytically, but a root-finding algorithm can rapidly find the shear strain γ required for failure for each value of the orientation θ . The orientation that requires the least amount of strain will be the orientation at which the system fails. Different combinations of μ^0 , μ' , and C will then produce different failure orientations. For high μ' , failure will first occur for $0 \leq |2\theta| \leq 90^\circ$, or $0 \leq \beta \leq 90^\circ$ (including conjugates). This means that for certain combinations of μ^0 , μ' , and C , (shallow) P-shears are produced before any R-shears (see Fig. (8B)).



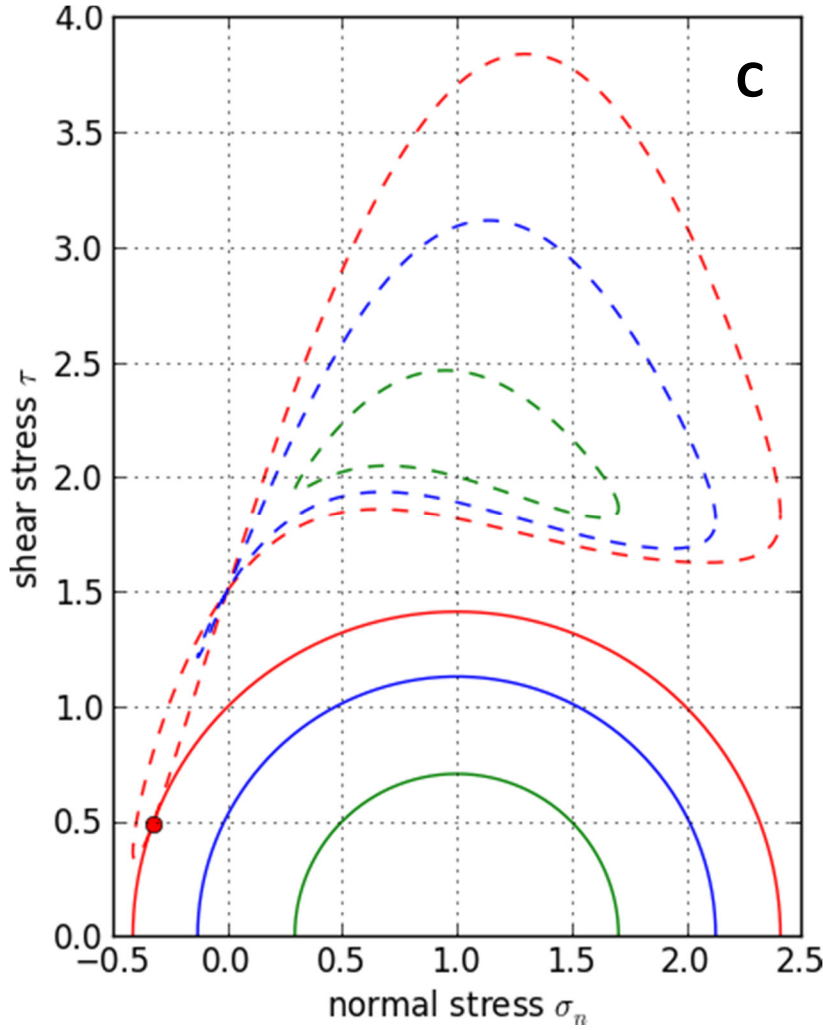


Figure 8: Mohr circles and their failure envelopes for various strains γ . The green circles and envelopes correspond to a strain of $\gamma = 0.5 \gamma_c$, the blue ones a strain of $\gamma = 0.8 \gamma_c$ and the red ones correspond to the critical amount of strain $\gamma = \gamma_c$ at which failure occurs.

A) An isotropic system with $\mu^0 = 0.6$, $\mu' = 0$ and $C = 0$. The envelopes are linear and independent of strain since $\mu = \mu^0$.

B) A strongly anisotropic system with $\mu^0 = 0.6$, $\mu' = 6.0$ and $C = 0$. The envelopes are now curved, rotated and a function of strain.

C) The same anisotropic system with strong cohesion. $\mu^0 = 0.6$, $\mu' = 6.0$ and $C = 1.5$.

Once the system has failed, a second failure plane is required to accommodate any two-dimensional strain. It is hereby assumed that the orientation of the second failure plane is the orientation that results in the lowest internal entropy production, i.e. the orientation that leads to the lowest macroscopic shear strength τ (de Groot & Mazur, 1984; see section 4.1). For the sake of clarity and convenience, the second shear band to form will from here on be called P-shear, although the second shear band orientation does not necessarily have to be a P-orientation.

The solution for the stress tensor σ_{ij} required for frictional sliding on two slip systems is given by (17). However, in the current situation only one slip plane has formed, the other plane has yet to form and may still have cohesion. Therefore, the right-hand side of (17) has to be rewritten:

$$\begin{bmatrix} (l_1 n_1)_R - \mu_R (n_1^2)_R & (l_1 n_2 + l_2 n_1)_R - 2\mu_R (n_1 n_2)_R & (l_2 n_2)_R - \mu_R (n_2^2)_R \\ (l_1 n_1)_P - \mu_P (n_1^2)_P & (l_1 n_2 + l_2 n_1)_P - 2\mu_P (n_1 n_2)_P & (l_2 n_2)_P - \mu_P (n_2^2)_P \\ 0 & 0 & 1 \end{bmatrix} \begin{bmatrix} \sigma_{11} \\ \sigma_{12} \\ \sigma_{22} \end{bmatrix} = \begin{bmatrix} 0 \\ C \\ \sigma_n \end{bmatrix} \quad (51)$$

Once the system has failed, the orientation and coefficient of friction of the failure plane are known. That leaves the orientation and friction coefficient of the P-shear plane as unknown variables. But since the friction coefficient is a function of shear band orientation and shear strain, the shear band orientation and shear strain can be varied in order to get the lowest macroscopic shear strength. Figure (9) shows the macroscopic shear strength τ against shear strain and P-shear orientation and clearly displays a minimum for any amount of strain and an P-angle $\beta \approx 10^\circ$. This implies that for a certain amount of shear strain, there is one angle β that results in the lowest shear strength.

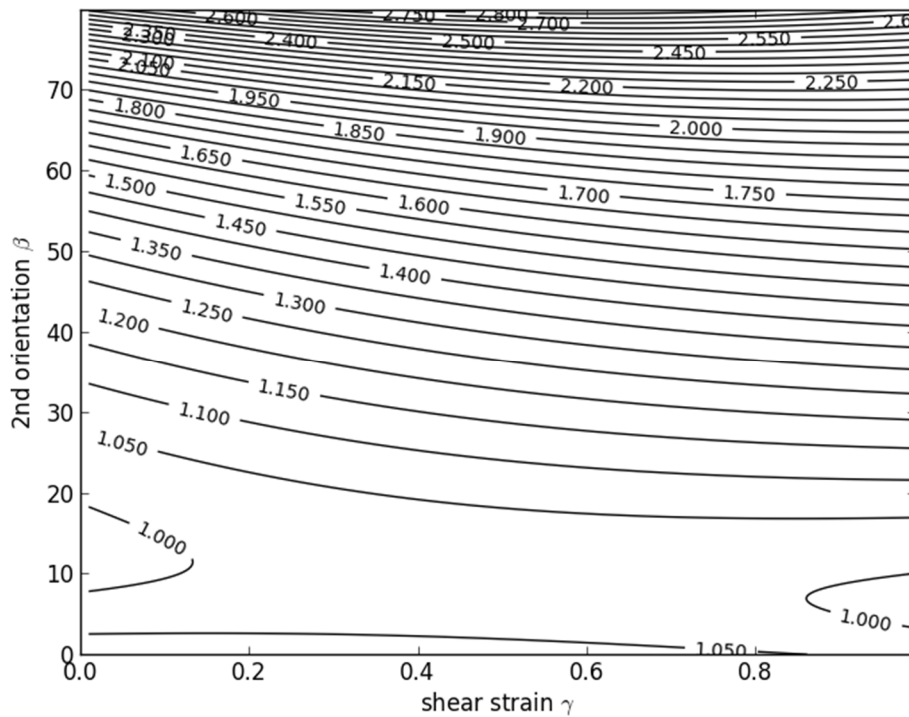


Figure 9: The contours of the macroscopic shear stress τ plotted against the angle of the P-shear orientation β and the applied shear strain γ . A minimum shear stress can be found for any γ around $\beta \approx 10^\circ$. For this example plot $\alpha = 165^\circ$, $\mu^0 = 0.6$, $\mu' = 2.0$, $C = 0.5$.

The next step is to determine how much shear strain will the system accommodate before the second shear band forms. From the Mohr-Coulomb failure of the first shear band the critical shear stress τ_c was obtained, and since a linear stress-strain relationship was assumed, obtaining the critical shear strain γ_c is trivial. This is the minimum amount of strain the system has to accommodate before any shear band can develop. When the shear stress obtained from solving (51) is lower than the shear stress required for Mohr-Coulomb failure of the first shear band, then stress does not need to increase any further to form the second shear band and no more strain needs to be accommodated by the system. In this case the second orientation will form at an angle where the macroscopic strength is at a minimum for a shear strain that is equal to the critical shear strain γ_c at which the system fails in a Mohr-Coulomb fashion.

When the shear stress obtained from solving (51) is higher than the shear stress required for Mohr-Coulomb failure, the system needs to accommodate more strain up to the point where stress obtained from (51) is met. Note that this extra strain will still be accommodated in the matrix and not in the first shear band that was formed, since a second shear band is required for multiple slip (von Mises, 1928; Taylor, 1938).

5.3 The formation of boundary shears as a result of activity on R- and P-shears

When R- and P-shears have formed, slip on these can accommodate any two-dimensional strain. The partition of strain into both shear bands is given by equation (24). Since the shear zone has a finite thickness, and since the shear bands are discrete in reality, there will be some strain incompatibility at the boundaries, i.e. strain accommodation by the shear bands will result in “gaps” or dilatant zones between the shear zone and the rigid country rock. These gaps will weaken the shear zone boundaries and if a certain critical amount of strain has been accommodated boundary shears may form as a result of the weakening. Here it is assumed that the gaps do not produce any (significant) macroscopic volumetric strain and that the local dilatation they produce is accommodated by local compaction within the gouge layer.

Let us define the sum of the activity of both shear bands as:

$$S \equiv \gamma_R + \gamma_P \quad (52)$$

It is now proposed that the coefficient of friction at the boundaries is a function of S , just like the coefficient of friction in the matrix is a function of the radius of the strain ellipse r :

$$\mu_B = \mu_B^0 \exp(-\mu'_B S) \quad (53)$$

It is then assumed that the boundary shears will form as a result of Mohr-Coulomb failure, i.e. failure occurs when the shear stress on the plane exceeds the frictional resistance. Reciting (47) and (48):

$$\tau_k = \frac{1}{2}(\sigma_1 - \sigma_2) \sin 2\theta \quad (47)$$

$$(\sigma_n)_k = \frac{1}{2}(\sigma_1 + \sigma_2) + \frac{1}{2}(\sigma_1 - \sigma_2) \cos 2\theta \quad (48)$$

In the case of boundary shears, $2\theta \approx 90^\circ$ (i.e. the shear band lies horizontal), so that (47) and (48) simplify to:

$$\tau_k = \frac{1}{2}(\sigma_1 - \sigma_2) \quad (55)$$

$$(\sigma_n)_k = \frac{1}{2}(\sigma_1 + \sigma_2) \quad (56)$$

This results in the following simplified failure criterion:

$$(\sigma_1 - \sigma_2) = \mu_B(\sigma_1 + \sigma_2) \quad (57)$$

or:

$$\mu_B = \frac{(\sigma_1 - \sigma_2)}{(\sigma_1 + \sigma_2)} \quad (58)$$

In this stage, the stress tensor is no longer linearly related to the strain, but is derived from solving (17) instead, which gives the following tensor:

$$\sigma_{ij} = \begin{bmatrix} \sigma_{11} & \tau \\ \tau & \sigma_n \end{bmatrix} \quad (59)$$

This tensor has the following eigenvalues:

$$\lambda = \frac{1}{2} \left[tr(\sigma_{ij}) \pm \sqrt{(tr(\sigma_{ij}))^2 - 4 \det(\sigma_{ij})} \right] \quad (60)$$

This simplifies (58) further, since:

$$\sigma_1 - \sigma_2 = \sqrt{(tr(\sigma_{ij}))^2 - 4 \det(\sigma_{ij})} \quad (61)$$

and:

$$\sigma_1 + \sigma_2 = tr(\sigma_{ij}) \quad (62)$$

So thus substituting (61) and (62) in (58) gives:

$$\mu_B = \frac{\sqrt{(tr(\sigma_{ij}))^2 - 4 \det(\sigma_{ij})}}{tr(\sigma_{ij})} = \mu_B^0 \exp(-\mu'_B S) \quad (63)$$

Solving for S gives:

$$S = \frac{1}{-\mu'_B} \ln \left(\frac{\sqrt{(tr(\sigma_{ij}))^2 - 4 \det(\sigma_{ij})}}{\mu_B^0 tr(\sigma_{ij})} \right) \quad (64)$$

From (24) it is easily derived that:

$$S = \gamma_R + \gamma_P = \frac{\gamma}{\sin(2\beta - 2\alpha)} [\sin(2\beta) + \sin(-2\alpha)] \quad (65)$$

Substituting (65) in (64) and solving for γ gives:

$$\gamma_{c,b} = \frac{\sin(2\beta - 2\alpha)}{-\mu'_B [\sin(2\beta) + \sin(-2\alpha)]} \ln \left(\frac{\sqrt{(tr(\sigma_{ij}))^2 - 4 \det(\sigma_{ij})}}{\mu_B^0 tr(\sigma_{ij})} \right) \quad (66)$$

where $\gamma_{c,b}$ is the critical strain at which boundary shears will form, measured from the moment both the R- and P-shears have formed.

5.4 The rotation of shear bands as a result of strain

Recall section 4.2 that the total deformation J_{ij} produced by N shear bands is given by:

$$J_{ij} = \sum_{k=1}^N (J_{ij})_k \quad (20)$$

and that ε_{ij} and ω_{ij} are given by:

$$\varepsilon_{ij} = \sum_{k=1}^N \frac{1}{2} (l_i n_j + l_j n_i)_k \gamma_k \quad (21)$$

$$\omega_{ij} = \sum_{k=1}^N \frac{1}{2} (l_i n_j - l_j n_i)_k \gamma_k \quad (22)$$

Suppose a system is forced to undergo an external deformation J_{ij}^X , then this must be accommodated by slip on N shear bands, and the externally imposed strain ε_{ij}^X must equal the internal strain ε_{ij}^I :

$$\varepsilon_{ij}^X = \varepsilon_{ij}^I = \sum_{k=1}^N \frac{1}{2} (l_i n_j + l_j n_i)_k \gamma_k \quad (67)$$

In a shear strain deformation regime, the following strain tensor applies:

$$\frac{1}{2} \begin{bmatrix} 0 & \gamma \\ \gamma & 0 \end{bmatrix} = \frac{1}{2} (l_i n_j + l_j n_i)_k \gamma_k \quad (68)$$

This will result in a rotation of the shear bands:

$$\omega_{ij}^I = \sum_{k=1}^N \frac{1}{2} (l_i n_j - l_j n_i)_k \gamma_k = \frac{1}{2} \begin{bmatrix} 0 & (l_1 n_2 - l_2 n_1)_k \gamma_k \\ (l_2 n_1 - l_1 n_2)_k \gamma_k & 0 \end{bmatrix} \quad (69)$$

whereas the external rotation is:

$$\omega_{ij}^X = \frac{1}{2} \begin{bmatrix} 0 & \gamma \\ -\gamma & 0 \end{bmatrix} = \frac{1}{2} \begin{bmatrix} 0 & (l_1 n_2 + l_2 n_1)_k \gamma_k \\ -(l_1 n_2 + l_2 n_1)_k \gamma_k & 0 \end{bmatrix} \quad (70)$$

Since $\omega_{ij}^I \neq \omega_{ij}^X$, a compensatory rotation ω_{ij}^C must take place, defined as:

$$\omega_{ij}^C \equiv \omega_{ij}^X - \omega_{ij}^I = \begin{bmatrix} 0 & (l_2 n_1)_k \gamma_k \\ -(l_2 n_1)_k \gamma_k & 0 \end{bmatrix} \quad (71)$$

Substituting (24), (1), and (2) in (71) and rewriting gives:

$$\omega_{ij}^c = \frac{\gamma}{2} \left(1 - \frac{\sin(2\beta) - \sin(2\alpha)}{\sin(2\beta - 2\alpha)} \right) \begin{bmatrix} 0 & 1 \\ -1 & 0 \end{bmatrix} \quad (72)$$

Any rotation matrix in general represents a rotation as follows:

$$R = \begin{bmatrix} \cos \theta & -\sin \theta \\ \sin \theta & \cos \theta \end{bmatrix} \quad (73)$$

Thus all material lines rotate over an angle θ described by:

$$\sin \theta = \frac{\gamma}{2} \left(\frac{\sin(2\beta) - \sin(2\alpha)}{\sin(2\beta - 2\alpha)} - 1 \right) \quad (74)$$

Since this rotation affects both α and β , $\frac{d\theta}{d\gamma}$ is not constant so that variations in α and β should be determined numerically with a small increment $d\gamma$. Note that this rotation applies to both the R- and P-shears in the same way, causing them both to rotate at the same rate.

5.5 The formation of Y-shears as a result of rotation of R- and P-shears

When the R-shears rotate into a Y-orientation, an undulatory network of R- and P-shears forms that may allow the formation of Y-shears inside the shear zone gouge, rather than at the boundary between the shear zone and the country rock. Similar to the approach that was used to predict boundary shear formation, one can reason that the coefficient of friction of a plane parallel to the shear zone boundary but situated inside the matrix, is reduced as the R-shears start to align with the Y-orientation. When the Y-shear has formed, it must have a coefficient of friction that is similar to that of the R-shear it formed from, and prior to Y-shear formation the friction coefficient must be higher than that of the R-shear. One possible solution is given by:

$$\mu_Y = \mu_R \exp(\mu'_Y [1 - \cos^2 \alpha]) \quad (75)$$

As α increases to 180° , μ_Y decreases to μ_R . Also, slip weakening of the R-shears will promote Y-shear formation. Similar to the derivation of the boundary shear done in section 5.3 earlier, a Y-shear will form when:

$$\mu_Y = \frac{\sqrt{(tr(\sigma_{ij}))^2 - 4 \det(\sigma_{ij}))}{tr(\sigma_{ij})} = \mu_R \exp(\mu'_Y [1 - \cos^2 \alpha]) \quad (76)$$

A value for μ'_Y in the order of 10 seems to yield Y-shears at realistic shear strains and R-shear orientations, though the exact value would be non-trivial to estimate.

6 Model results and discussion

In this section the results of the model are compared with observations. In this way, we attempt to test the following hypotheses. Early calculations revealed that the model's features could not be produced without making certain assumptions, which motivated the formulation of these hypotheses:

- 1) The matrix anisotropy affects the order of shear band activation (R-shears activate before P-shears or vice versa).
- 2) The friction coefficient parameters, μ^0 and μ' , and the macroscopic properties c and σ_n , strongly affect:
 - a. the orientations at which the shear bands form,
 - b. the amount of strain to be accommodated to activate both shear bands and
 - c. the rheology of both the macro scale fault zone and the internal shear bands.
- 3) The shear bands rotate as a result of strain accommodation by the shear bands itself.

6.1 The effect of anisotropy on the order of activation and orientations of R- and P-shears

Since the coefficient of friction μ is directionally dependent in a system where $\mu' > 0$, it is expected that the orientations of the shear bands that are activated first and second are directly affected by μ . In addition, other parameters are involved: cohesion C , stress-strain coefficient c and the macroscopic normal stress σ_n . The plots presented in Fig. (10) all show the contour lines of the orientation of the activated shear band w.r.t. the shear zone boundary against the friction coefficient parameters μ^0 and μ' for various values of C . Quickly scanning the overall trends seen in these plots, e.g. in Fig. (10A) for which $C = 0$, it can already be concluded that the predicted orientations will fall into two regimes: in the first, low anisotropy regime roughly for $\mu' < 4$, the orientations of the first shear band lie in the range of observed R-orientations, i.e. $160^\circ < \alpha < 175^\circ$ (or $5^\circ < \alpha < 20^\circ$ measured clockwise). When the system is isotropic ($\mu' = 0$) the angles predicted exactly match those predicted by the Mohr-Coulomb failure theory (eqn. (44)).

The second, high anisotropy regime ($\mu' > 4$) predicts the first shear band to form at shallower angles, typically less than 10° , and oriented in the P-orientation. These regimes are also found in the

orientation of the shear band that forms second. Fig. (10B) ($C = 0$) only shows reliable results in the top-left corner of the plot, for the rest of the plot no minimum τ was found other than $\tau = -\infty$, thus no preferred orientation of the second shear band could be obtained. This suggests that some cohesion is required to actually get a preferred orientation for most combinations of μ^0 and μ' . If no second shear band would form, it is reasonable to assume that after the first shear band has formed, only Y- and boundary shears can form. Keller et al. (1997) report preferred P-shear (typically $10^\circ \leq \beta \leq 15^\circ$) and Y-shear development over R-shears in the Rambla de Granatilla gouge zone of the Carboneras fault system. They reproduced their observations carried out in the field by using a clay box model analogue, where the unconsolidated clay consisted of mostly kaolinite. Their box model results would coincide with this thesis model results for a combination of $\mu' > 4$ and $C = 0$. Fig. (10D) ($C = 0.5$) shows that adding some cohesion to the system would result in a preferred orientation for the second shear band.

The angles found in the first regime ($\mu' < 4$) fall in a wide range $-15^\circ < \beta < 40^\circ$, though only a range of $10^\circ < \beta < 35^\circ$ is feasible for values of μ^0 expected to be found in nature. The second regime ($\mu' > 4$) predicts shear bands in an R-orientation ($160^\circ < \alpha < 180^\circ$). Increasing the cohesion to relatively high values ($C = 1.0$; Fig. (10E and F)) adds a third regime for high values of μ^0 predicting very steep shear band orientations. Closer inspection of the stresses involved in this regime reveals that failure in this regime only occurs in a tensile state of stress (see Fig. (8C) for an example) and is therefore very unlikely to represent natural shear zones. The range of P-shear orientations shifts towards higher values by about 5° compared to a system with $C = 0.5$ and equal values of μ^0 and μ' .

Since the P-shears were defined to be oriented at $0 < \beta \leq 90^\circ$ and the R-shears to be oriented at $90^\circ < \alpha \leq 180^\circ$, the orientations of the first and second shear bands formed now also provide the order of activation of R- and P-shears. Based on Fig. (10C and D), it can be concluded that for low anisotropy systems ($\mu' < 4$) the R-shears activate first, and that for high anisotropy systems P-shears activate first. If P-shears activate first, their predicted orientations are much shallower than when they are activated second.

When σ_n and c are varied, an interesting trend emerges: for $\sigma_n = 1.0$ and $c = 2.0$ (Fig. (12A and B)), the μ' that marks the high-anisotropy regime shifts towards double values. On the other hand, when $\sigma_n = 2.0$ and $c = 1.0$ (Fig. (12C and D)), the μ' that marks the high-anisotropy regime shifts towards values that are only half the values when $\sigma_n = 1.0$ and $c = 1.0$. For $\sigma_n = 2.0$ and $c = 2.0$ (Fig. (14E

and F)), the μ' remains at the same values as for when $\sigma_n = 1.0$ and $c = 1.0$ (Fig. (10E and F)). This suggests a linear relationship between μ' for which a regime shifts and σ_n and c .

The main difference between Figures (10F) and (12F) is the predicted orientations. For both situations $\frac{\sigma_n}{c} = 1$, but in the latter the normal stress is higher than the cohesion C , whereas in the former the $\sigma_n = C$. Equation (16) and its expansion (17) show the relative importance of σ_n and C : if σ_n in the right-hand side of (17) changes relative to C , the relative proportions of the components of σ_{ij} change. When the σ_n and C vary in an absolute sense, but not in a relative sense, the proportions of σ_{ij} remain the same and the components are merely multiplied by a constant number. The orientations of the shear band to form second will therefore only change if σ_n changes relative to C . This is further demonstrated by the comparison of Figures (10D) ($\sigma_n = 1.0, c = 1.0, C = 0.5$) and (12F) ($\sigma_n = 2.0, c = 2.0, C = 1.0$): the solutions within the low-anisotropy regime are identical.

Haines et al. (2013) conducted a shear deformation experiment with montmorillonite at 20 MPa normal stress and found that experiments stopped at peak stress had R-shear angles between $9^\circ - 14^\circ$ (measured clockwise) and P-shear angles between $10^\circ - 35^\circ$ (measured counter-clockwise). Based on their mechanical data (see Fig. (11A)), one can conclude that $c = 9.2$ and $\sigma_n = 20$, with the additional information that the maximum apparent coefficient of friction is found to be 0.46, with a drop of about 0.6 before steady state is reached. With these constraints in mind, one can tune the model parameters in an attempt to match the observed shear band orientations macroscopic rheology. When this is done, it is found that this combination of α and β can only be obtained for a cohesion $C > 4.0$, which is too high for fault gouge, especially since gouge is considered incohesive by definition (Brodie et al., 2002). This definition is supported by experimental observations (Scott et al., 1994; Grøneng et al., 2009). Grøneng et al. (2009) found cohesive strengths typically less than 0.2 MPa for gouges derived from a wide range of materials. This means that, in order to fit the experimental results of Haines et al. (2013), other assumptions have to be made. It might be that the assumption that μ^0 and μ' are the same for both R- and P-shears is incorrect, since they tend to form by different mechanisms. Alternatively, the R-shears may rapidly weaken (i.e. reduce μ^0) after formation. If the R-shears have, for instance, different μ^0 than P-shears do, the model can produce a wider range of shear band orientations for a given set of constraints. For instance, Fig. (11B) was rendered with the following set of parameters:

$$\mu_R^0 = 0.45, \quad \mu_P^0 = 0.60, \quad \mu' = 0.5, \quad C = 0.1$$

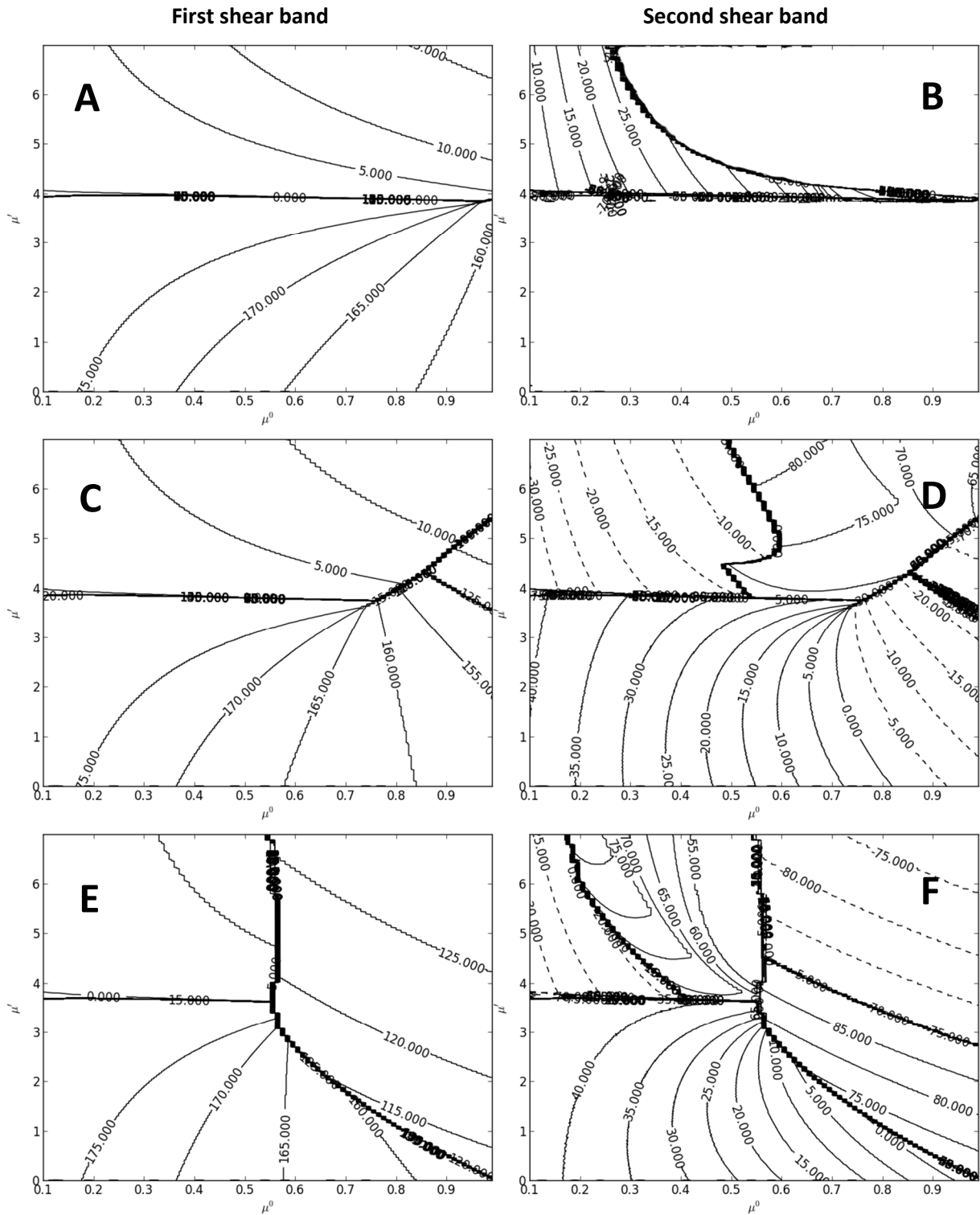


Figure 10: The contours of the orientation of the activated shear bands plotted against the isotropic part of the friction coefficient μ^0 (x-axis) and the sensitivity to matrix anisotropy μ' (y-axis). Solid contour lines represent positive values, dashed lines negative values. The angles are measured counter-clockwise relative to the shear zone boundary. For all plots $c = 1$ and $\sigma_n = 1$, and the contour lines have 5° increments. **A and B)** $C = 0$. For large portions of B) there was no minimum found for τ other than $\tau = -\infty$, therefore no preferred orientation for the second shear band was obtained except for the top-left portion; **C and D)** $C = 0.5$. Now that cohesion has been added to the system, a preferred orientation for the second shear band can be obtained; **E and F)** $C = 1.0$.

In addition, a maximum of 30% slip weakening and no Y- or boundary shear activity was assumed. The resulting R- and P-shear orientations are $\alpha = 171^\circ$, $\beta = 19^\circ$, which is in the range of the observed orientations. Furthermore, the stress-strain evolution is quite similar to the mechanical data from the experiments that were used for calibration. However, only the results of experiments that display strain weakening can be reproduced. Processes such as cross-slip may result in work hardening observed during plastic deformation of crystals (Asaro & Rice, 1977) and similarly slip system interference or other micromechanical processes, which are not included in the model, may result in the work hardening behaviour observed in the experiments of Haines et al. (2013).

In summary, the model predicts that the R-shears generally activate first, but for a restricted combination of the frictional parameters μ^0 and μ' , the P-shears are found to form prior to the R-shears. The shear band orientations as observed in experiments can only be reproduced by the model if the material is assumed to have a high cohesive strength, or if it is assumed that the R- and P-shears can have different frictional parameters, i.e. $\mu_R^0 \neq \mu_P^0$.

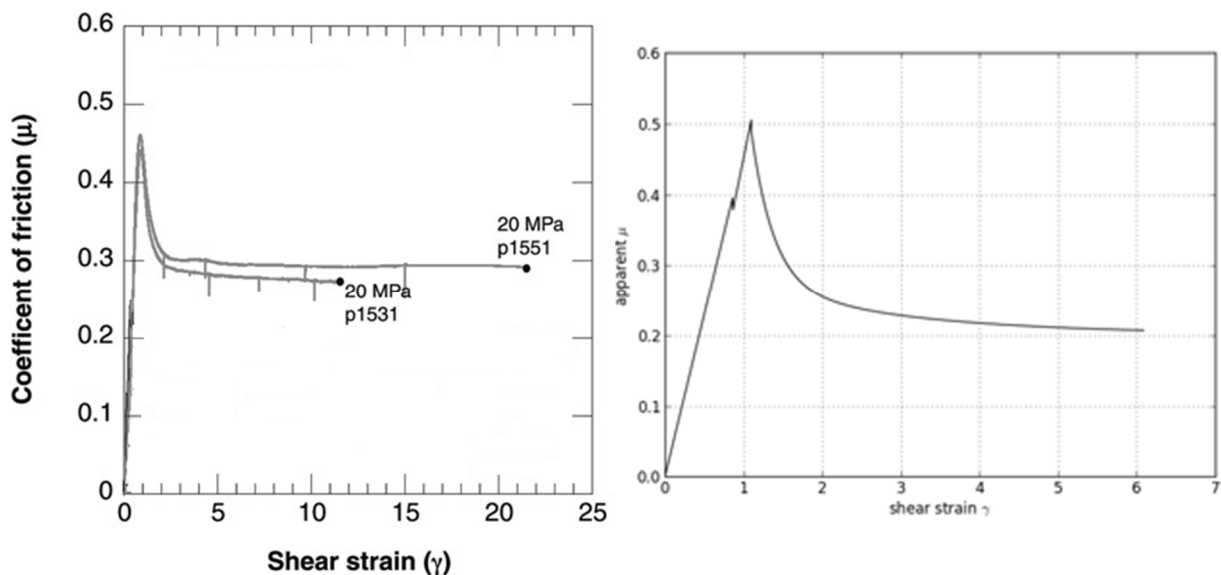


Figure 11: A) Mechanical data from a montmorillonite shear deformation experiment at $\sigma_n = 20$. Modified from Haines et al. (2013) B) The predicted macroscopic shear stress τ divided by the normal stress σ_n , plotted against shear strain. See text for a description of the parameters used to render this plot.

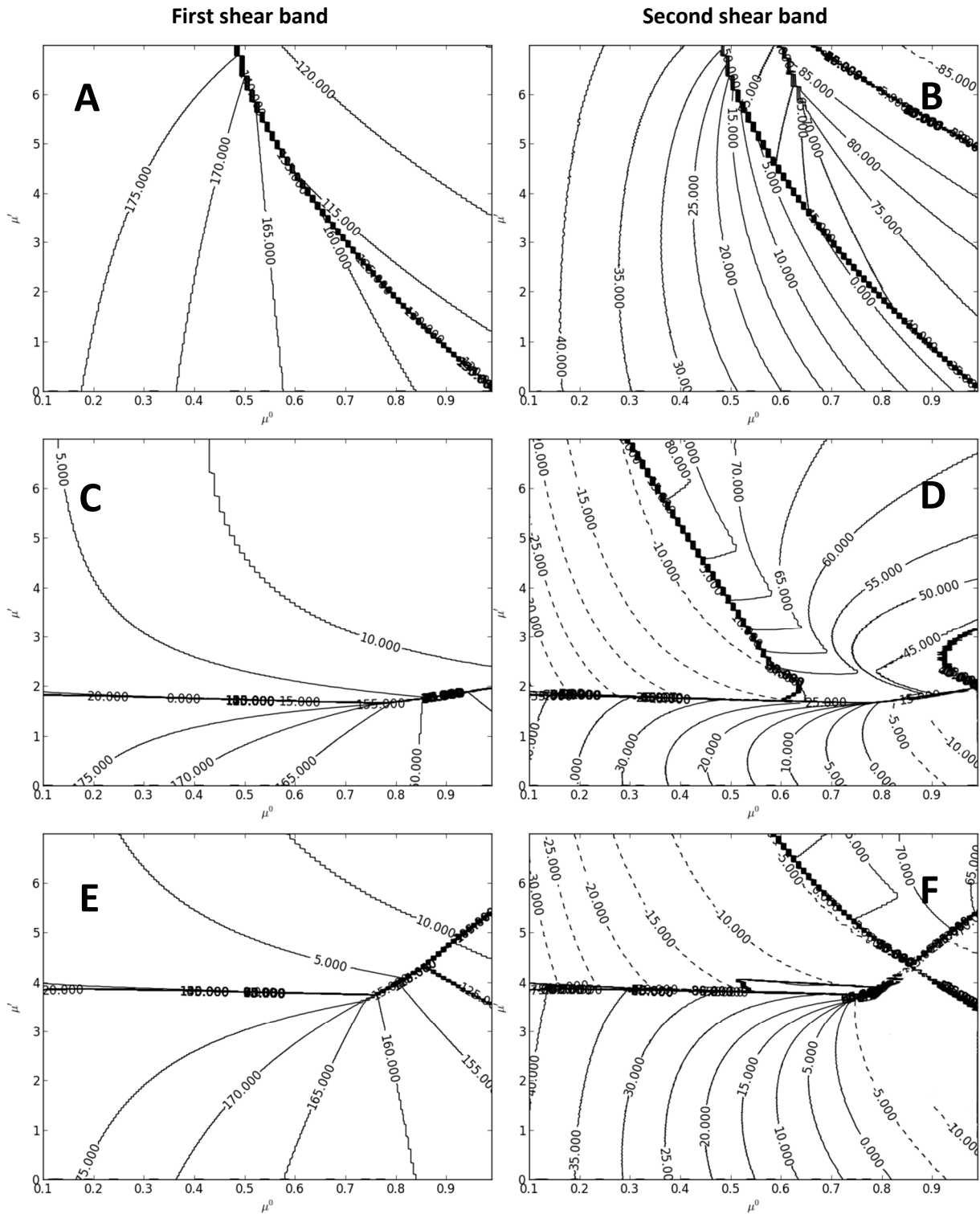


Figure 12: The contours of the orientation of the activated shear bands plotted against the isotropic part of the friction coefficient μ^0 (x-axis) and the sensitivity to matrix anisotropy μ' (y-axis). Solid contour lines represent positive values, dashed lines negative values. The angles are measured counter-clockwise relative to the shear zone boundary. For all plots $C = 1.0$, and the contour lines have 5° increments. **A and B)** $\sigma_n = 1.0$ and $c = 2.0$. The boundary between the low- and high anisotropy regimes lies around $\mu' = 8.0$ (off chart). **C and D)** $\sigma_n = 2.0$ and $c = 1.0$. **E and F)** $\sigma_n = 2.0$ and $c = 2.0$. See text for discussion.

6.2 The effect of anisotropy on the shear strain required for activating R- and P-shears

Based on a linear $\sigma - \varepsilon$ relationship prior to Mohr-Coulomb failure, the model predicts a certain amount of inelastic shear strain before the stress required to activate the first shear band is reached. The second shear band may form instantaneously with the first one, or it may require more shear strain to reach a higher state of stress. We define the relative activation strain $\hat{\gamma}$ as:

$$\hat{\gamma} \equiv \frac{\gamma_2}{\gamma_1} \quad (77)$$

where γ_1 is the shear strain needed to activate the first shear band, and γ_2 the strain needed for the second shear band. The quantity $\hat{\gamma}$ expresses the additional strain required to activate the second shear band relative to the strain required to activate the first shear band. If the second shear band forms synchronously with the first one, $\hat{\gamma} = 1$. If more strain is required to activate the second shear band, $\hat{\gamma} > 1$. Fig. (13) shows $\hat{\gamma}$ plotted against the two parameters of μ . There is one region for $\mu' < 3$ and $\mu^0 > 0.45$ where the system needs to accommodate more strain in order to activate the second shear band. The domains of this area varies with C , c and σ_n , though the trend remains that for low μ' and high μ^0 more strain needs to be accommodated. Haines et al. (2013) report phyllosilicates to lie in a P-orientation as soon as R-shears have formed, even when the R-shears have not yet fully propagated through the shear layer, indicating that P-shears form synchronously with R-shears, as is predicted by this model. Only in relatively strong materials ($\mu^0 > 0.6$) the P-shears require more strain (i.e. higher stress) to form.

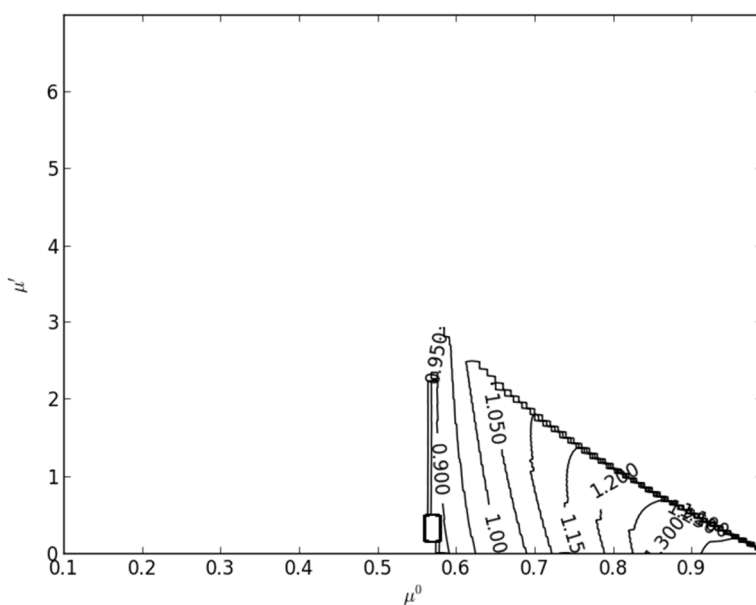


Figure 13: The relative activation strain $\hat{\gamma}$ plotted against μ^0 and μ' . For $\mu' < 3$ and $\mu^0 > 0.45$ additional strain is required to activated the second shear band. For this plot $C = 1$, $c = 1$ and $\sigma_n = 1$

6.3 The effect of anisotropy on the initial coefficients of friction of activated R- and P-shears: effects and consequences

Up to the shear strain at which the shear bands form, the strain ellipse evolves and so does the directionally dependent coefficient of friction inside the shear zone (for $\mu' > 0$). Once a shear band has formed, its friction coefficient is fixed, which can be plotted against μ^0 and μ' (Fig. (14)). For the parameters used in Fig. (14) ($C = c = \sigma_n = 1$) and the regime bounded by $0 < \mu' \leq 4$, the first shear band to form is an R-shear, and the second a P-shear. Examining Fig. (14) for these constraints reveals that the coefficient of friction of the P-shears is less than that of the R-shears, implying that the P-shears are weaker than R-shears for any combination of μ^0 and μ' . This observation can be explained by considering the orientation of the strain ellipse relative to the R- and P-shear orientations: the P-orientation lies more or less parallel to the long axis of the strain ellipse, whereas the R-orientation lies close to perpendicular to it, resulting in a low friction coefficient for the P-shears and a high friction coefficient for the R-shears (see eqn. (37)). For an isotropic system ($\mu' = 0$) the friction coefficients of both shear bands is identical.

The macroscopic coefficient of friction is somewhat higher than expected from experimental observations. Haines et al. (2013) report peak strengths typically up to 0.5 for montmorillonite, crushed illite shale and natural chlorite gouge. Logan (2007) obtained friction coefficients for various material quartz contents (Fig. (14D)). Even for the highest amounts of quartz the (macroscopic) friction coefficient does not exceed 0.6, and higher clay contents give friction coefficients that are much lower than that. If the model were to be calibrated using the macroscopic friction, the model predictions for the shear band orientations would yield very low angle R-shears ($\alpha > 175^\circ$) and high angle P-shears ($\beta > 40^\circ$). Thus the coefficient of friction is another indication that one of the assumptions that were made is incorrect. Again, if the system is allowed to have different μ^0 for both shear bands, solutions can be obtained that better predict the shear band orientations and macroscopic friction, as is demonstrated by Fig. (12).

Concluding, one can state that the P-shears are frictionally weaker than the R-shears assuming $\mu_R^0 = \mu_P^0$, but that the same assumption results in a macroscopic strength that is higher than is typically observed in experiments.

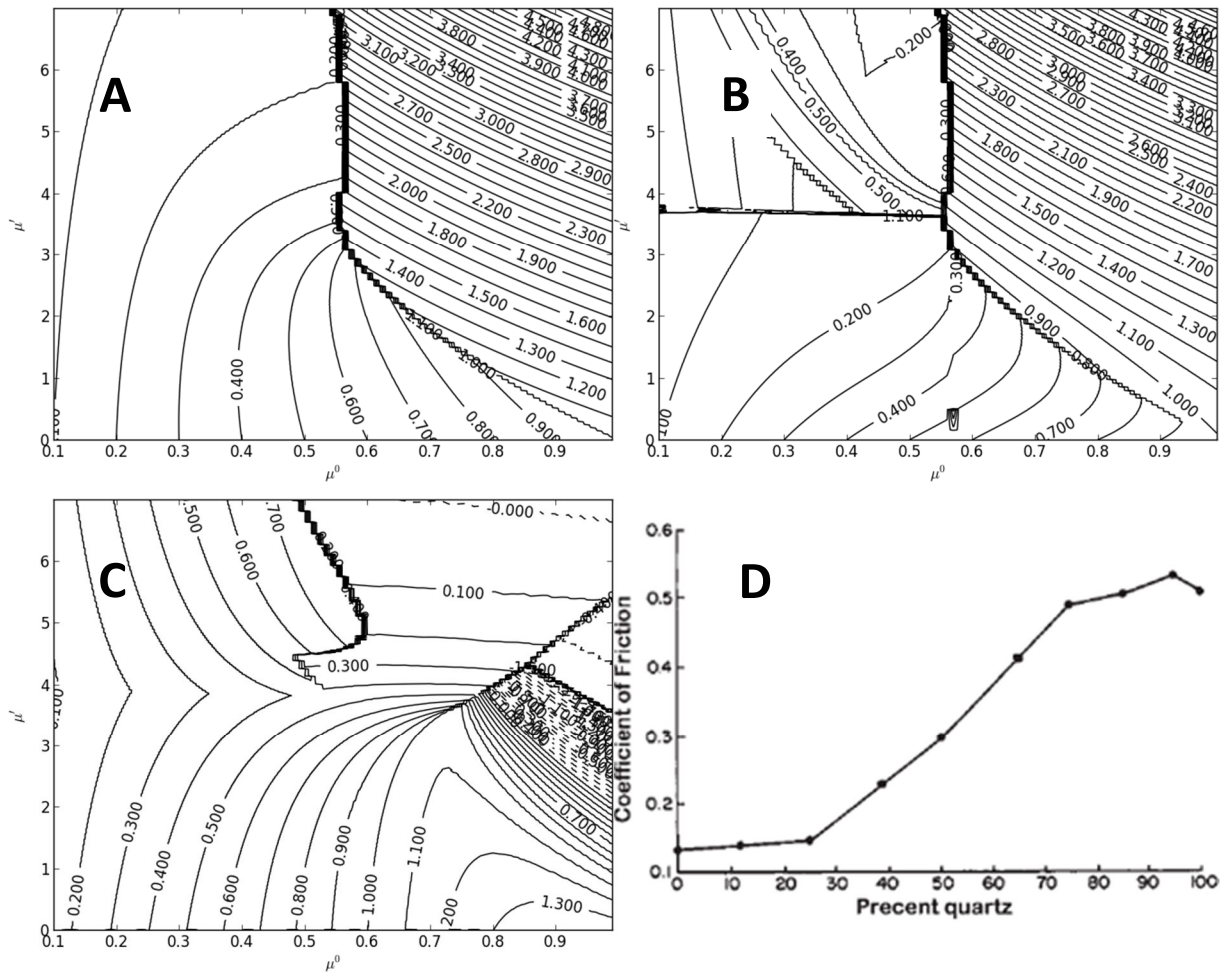


Figure 14: The coefficient of friction μ_k of the first shear band (A), the second shear band (B) and the macroscopic coefficient of friction directly after the shear bands have formed (C), plotted against μ^0 and μ' . For $0 < \mu' \leq 4$ the friction coefficient of the second shear band (P-shear) is less than that of the first shear band (R-shear). A) and B) show the third regime of tensile stresses for high μ^0 . $C = 1$, $c = 1$ and $\sigma_n = 1$. D) shows the experimentally obtained coefficients of friction as a function of the quartz content (from Logan, 2007)

6.4 The rotation of shear bands and the orientation of σ_1

Fig. (15) shows the predicted rotation of the shear bands against strain for a moderately anisotropic system with low cohesive strength width fixed parameters $\mu^0 = 0.5$, $\mu' = 1.0$ and $C = 0.5$. It shows that the R-shears rotate towards a Y-orientation and their angles decrease by 10° in about 4 – 6 units of shear strain, which is similar to what is reported by Haines et al. (2013). However the P-shears rotate by a similar amount in the same direction, while it is reported that in lab experiments they remain in a fixed orientation (Tchalenko & Ambraseys, 1970; Logan et al., 1979; Haines et al., 2013). The rotation of Fig. (15) is a reflection of ω_{ij} as was obtained in section 5.4. Since ω_{ij} applies to all material lines, both shear bands will rotate at the same rate in the same direction.

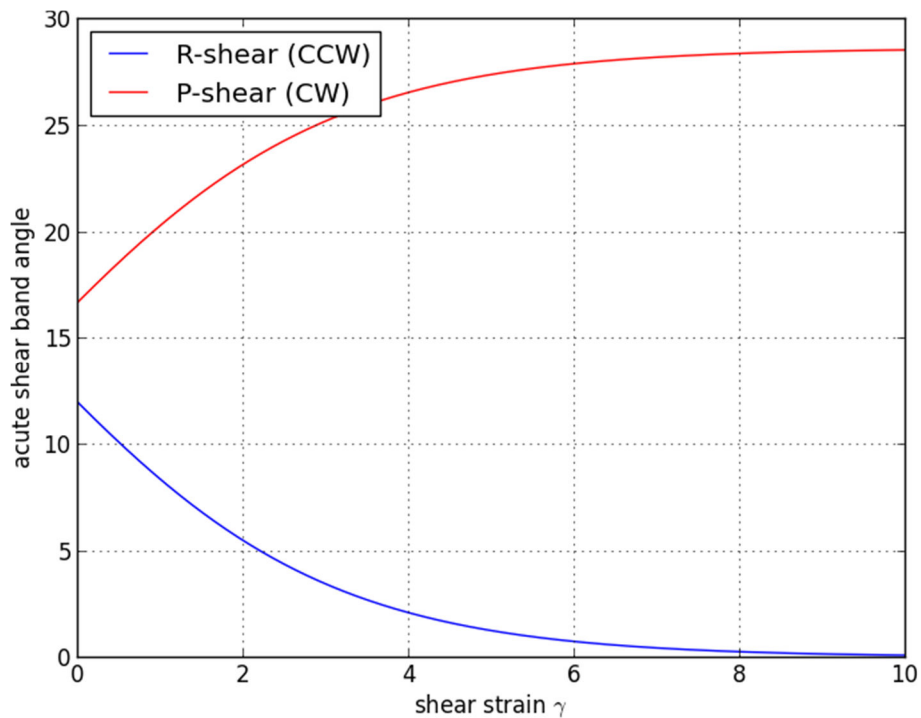


Figure 15: The acute angle between the R- and P-shears and the shear zone boundary plotted against shear strain γ . The R-shear rotates towards a Y-orientation as observed, and the P-shear rotates by the same amount. For this plot $\mu^0 = 0.5$, $\mu' = 1.0$, $C = 0.5$, $c = 1$ and $\sigma_n = 1$.

Stock (1992) presented a strain model for the rotation of fabric elements in a simple shear deformation, which predicts the antithetic rotation of material lines. The difference with the presented model is that Stock (1992) accommodated the shear strain in the matrix, causing rotation of the microlithons, whereas the presented model accommodates strain in the two shear bands, where the rotation has geometrical causes. Both models are not mutually exclusive though: Stock (1992) predicts rotation prior to R- and P-shear formation, the presented model predicts the rotation after shear band formation.

Several studies have suggested that P-shears might orient themselves perpendicular to orientation of the maximum principle stress σ_1 (Tchalenko & Ambraseys, 1970; Logan et al., 1979; Haines et al., 2013). Ideally, σ_1 would be oriented at a 45° angle w.r.t. the shear zone boundary, which would result in a P-orientation of $\beta = 45^\circ$. For shallower P-orientations $\beta < 20^\circ$ as reported by Logan et al. (1979) and Logan & Rauenzahn (1987), σ_1 would have to lie at a very steep angle of about 70° . Also, if it is assumed that eqn. (16) applies to real-world shear zones, then the σ_1 -orientation must be a function of the shear band orientations and friction coefficients. When R-shears rotate, the state of stress will change immediately, changing the orientation of σ_1 and the orientation of P-shears.

Therefore, if the R-shears rotate, then the P-shears have to rotate as well. This reasoning suggests some other, yet undetermined mechanism causes the P-shears to remain fixed. It should be confirmed though whether the rotation/fixation of the shear bands reported by Haines et al. (2013) is a result of shear strain accommodated by the shear bands, or a result of thinning of the sheared layer due to extrusion of gouge material at the ends of the forcing blocks of the testing apparatus (Scott et al., 1994). The mechanical data has been corrected for this effect, but the SEM images from which the shear band orientations were derived may not have been adjusted to compensate for the geometric thinning. The thinning would promote R-shear rotation, but counteract the antithetic P-shear rotation. Also, since the apparatus used by Haines et al. (2013) and most apparatuses in general do not preserve volume during the experiments due to extrusion of mass, equation (20) and the equations derived from it may not apply to the results of the experiments. For an experimental set-up where volume is preserved, it may be found that P-shears do rotate at the same rate as the R-shears rotate.

Additionally, the possibility that P-shears may continuously form in the orientation producing the lowest macroscopic strength (and overprinting all previous orientations) was investigated. It was found that when the R-shears rotate, the P-orientation producing the lowest macroscopic strength rotates at exactly the same rate in the same direction. In other words, if the P-shears would continuously reform and reorient themselves, the resulting P-orientation would be exactly the same as when the P-shears would rotate without reforming. This implies that overprinting does not keep the P-shears in a fixed orientation.

In summary, the model predicts that both the R-shears and the P-shears rotate at the same rate against the direction of shear. The rotation of the R-shears is observed in experiments, but the same experiments show that the P-shears remain in a fixed orientation. This may be related to extrusion of sample material during shear deformation, violating the assumption of constant volume that was made in order to apply equation (20) to the model fault zone.

6.5 The effect of an anisotropic starting material

For the derivation of the anisotropy evolution in this thesis, a random distribution of mineral grain orientations was assumed, so that the material is isotropic before any shear strain is applied. However, it should be noted that when the starting mineral foliation is parallel to the direction of shear, the mineral grains will not rotate towards the long axis of the strain ellipse and the resulting anisotropy will be different from what was derived earlier in this thesis (section 5.1). More generally, a strong initial foliation, such as observed in Haines et al. (2013) for instance, as well as discrete heterogeneities, such as large clasts, can strongly affect the formation and orientation of crenulations, and localisation behaviour (Cosgrove, 1976; Hanmer, 1979). In order to apply the current model to natural fault zones, initial foliations and heterogeneities must be taken into account.

7 Conclusions and Recommendations for future work

Based on the model outcomes, the following can be concluded:

- 1) The model is capable of predicting shear band orientations that lie in the range of observed orientations, although comparison of orientations with those found in specific experiments reveals that either anomalously high cohesion is required to account for both the R- and P-shear angles, or one of the assumptions is incorrect. A candidate for an incorrect assumption could be the one stating that both R- and P-shear share the same μ^0 (and possibly μ'), although no physical basis for this is proposed.
- 2) The model predicts macroscopic coefficients of friction that are higher than expected from observations, though no extraordinarily high friction coefficients are produced for the range of expected friction parameters (μ^0 and μ'). Again, if the assumption stating that both R- and P-shear share the same friction parameters proves to be false, the model results fit experimental results better.
- 3) The model predicts the order of shear band activation that is typically observed: R-shears activate synchronously with or a little earlier than P-shears.
- 4) The model predicts an antithetic rotation of both the R- and P-shears, where the R-shears rotate asymptotically towards a Y-orientation, and the P-shears rotate the same amount in the same direction.
- 5) Y-shears, along with boundary shears, can be produced by strain accommodation on the R- and P-shears. Activity of the shear bands will cause rotation of the R-shears towards a Y-orientation, allowing Y-shear formation, and will cause damage at the boundary between the shear zone and the country rock, promoting boundary shear formation. Which shear band forms first, if at all, depends on the choice for the model parameters.
- 6) When the shear bands' friction coefficient parameters are chosen independently (i.e. $\mu_R^0 \neq \mu_P^0$), the stress-strain evolution of experiments can be reproduced within reasonable accuracy.

- 7) Currently the model only produces macroscale strain weakening rheology. In plastic deformation of crystals, processes such as cross-slip may result in work hardening (Asaro & Rice, 1977) and similarly slip system interference or other micromechanical processes, which are not included in the model, may result in the work hardening behaviour observed in the experiments of Haines et al. (2013).

One of the most important points for improvement of the model is quantifying the rotation of the P-shears as a result of non-isovolumetric shear strain accommodation by R- and P-shears. The model predicts rotation of the P-shears at the same rate as the R-shears do, whereas observations suggest that P-shears remain in a fixed orientation, even though R-shears do rotate. However, one of the key assumptions of the model is that any deformation does not lead to a change in volume, whereas this assumption generally is not satisfied in experiments due to the loss of sample material. These experiments may yield results that are different from the model predictions.

A second recommendation is to further investigate the microphysical basis of the parameters μ^0 and μ' of the shear bands' friction coefficient μ_k . The model results suggest that in order to fit experimental observations, μ^0 might be different for R- and P-shears and may therefore reflect the properties of the mechanism of formation of the shear bands, rather than material properties, although there is no solid basis for this suggestion. Another possibility would be that the R-shears rapidly weaken after formation, thus reducing μ_R^0 relative to μ_P^0 .

A third possible improvement would be to include more details in the relation between stress and shear band formation. Right now the model predicts somewhat higher peak stresses than observed, since it predicts the state of stress at which R-shears fully propagate the sheared layer. In reality R-shears can (partially) form due to local stress variations and time-dependent behaviour such as micro-cracking. The peak stress will therefore be lower than predicted by the current model. Also, the model can only predict strain weakening after R- and P-shears have formed, but experiments where work hardening is observed are common.

Lastly, an important input for the model would be the constraints on model parameters, especially on μ^0 and μ' . The model's predictive capabilities can be tested by identifying the ranges in which these parameters can occur and comparing the range of feasible shear band orientations with observations.

Acknowledgement

I'd like to thank my supervisor, Chris Spiers, for the valuable discussions we've had during our (lunch) meetings, and time he invested in my thesis project. Without his help I wouldn't have gotten nearly as far as I did.

References

- Asaro, R.J. & J.R. Rice. (1977), Strain localization in ductile single crystals. *Journal of the Mechanics and Physics of Solids* 25(5), pp.309-338.
- Bartlett, W.L., M. Friedman & J.M. Logan. (1981), Experimental folding and faulting of rocks under confining pressure Part IX. Wrench faults in limestone layers. *Tectonophysics* 79(3-4), pp.255-277.
- Bishop, J.F.W. & R. Hill. (1951), A theory of the plastic distortion of a polycrystalline aggregate under combined stresses. *Philosophical Magazine* 42, pp.414-427.
- Brodie, K., D. Fettes, B. Harte et al. (Web version of 31-10-2002), Structural terms including fault rock terms. A proposal on behalf of the IUGS Subcommittee on the Systematics of Metamorphic Rocks
- Byerlee, J., V. Mjachkin, R. Summers et al. (1978), Structures developed in fault gouge during stable sliding and stick-slip. *Tectonophysics* 44(1-4), pp.161-171.
- Chaves, E.W.V. (2013), *Notes on Continuum Mechanics*. Springer Netherlands
- Cosgrove, J.W. (1976), The formation of crenulation cleavage. *Journal of the Geological Society* 132(2), pp.155-178.
- de Groot, S.R. & P. Mazur. (1984), *Non-equilibrium thermodynamics*. Dover Publications, Inc., New York
- den Hartog, S.A.M., C.J. Peach, D.A.M. de Winter et al. (2012), Frictional properties of megathrust fault gouges at low sliding velocities: New data on effects of normal stress and temperature. *Journal of Structural Geology* 38, pp.156-171.
- Fossen, H. (2010), *Structural Geology*. Cambridge University Press
- Grøneng, G., B. Nilsen & R. Sandven. (2009), Shear strength estimation for Åknes sliding area in western Norway. *International Journal of Rock Mechanics and Mining Sciences* 46(3), pp.479-488.
- Haines, S.H., B. Kaproth, C. Marone et al. (2013), Shear zones in clay-rich fault gouge: A laboratory study of fabric development and evolution. *Journal of Structural Geology* 51, pp.206-225.
- Haines, S.H., B.A. Van Der Pluijm, M.J. Ikari et al. (2009), Clay fabric intensity in natural and artificial fault gouges: Implications for brittle fault zone processes and sedimentary basin clay fabric evolution. *Journal of Geophysical Research B: Solid Earth* 114(5)
- Hanmer, S.K. (1979), The role of discrete heterogeneities and linear fabrics in the formation of crenulations. *Journal of Structural Geology* 1(1), pp.81-"87,89-91".
- Hasan, A. & K. Alshibli. (2012), Three dimensional fabric evolution of sheared sand. *Granular Matter* 14(4), pp.469-482.
- Keller, J.V.A., S.H. Hall & K.R. McClay. (1997), Shear fracture pattern and microstructural evolution in transpressional fault zones from field and laboratory studies. *Journal of Structural Geology* 19(9), pp.1173-1187.
- Lehner, F.K. & J. Bataille. (1984), Nonequilibrium thermodynamics of pressure solution. *Pure and Applied Geophysics PAGEOPH* 122(1), pp.53-85.
- Lister, G.S., M.S. Paterson & B.E. Hobbs. (1978), The simulation of fabric development in plastic deformation and its application to quartzite: The model. *Tectonophysics* 45(2-3), pp.107-158.

- Logan, J., M. Freidman, M. Higgs et al. (1979), Experimental studies of simulated fault gouge and their application to studies of natural fault zones. In: Proc. Conf. VIII, Analysis of Actual Fault Zones in Bedrock. U.S. Geological Survey, Menlo Park, CA, pp.305-343.
- Logan, J.M. (2007). The progression from damage to localization of displacement observed in laboratory testing of porous rocks Retrieved 20 September 2013.
- Logan, J.M., C.A. Dengo, N.G. Higgs et al. (1992). Chapter 2 Fabrics of Experimental Fault Zones: Their Development and Relationship to Mechanical Behavior Retrieved 24 October 2013.
- Logan, J.M. & K.A. Rauenzahn. (1987), Frictional dependence of gouge mixtures of quartz and montmorillonite on velocity, composition and fabric. *Tectonophysics* 144(1-3), pp.87-108.
- Mandl, G., L.N.J. de Jong & A. Maltha. (1977), Shear zones in granular material - An Experimental Study of Their Structure and Mechanical Genesis. *Rock Mechanics Felsmechanik Mécanique des Roches* 9(2-3), pp.95-144.
- Pietruszczak, S. & Z. Mroz. (2000), Formulation of anisotropic failure criteria incorporating a microstructure tensor. *Computers and Geotechnics* 26(2), pp.105-112.
- Pietruszczak, S. & Z. Mroz. (2001), On failure criteria for anisotropic cohesive-frictional materials. *International Journal for Numerical and Analytical Methods in Geomechanics* 25(5), pp.509-524.
- Power, W.L. & T.E. Tullis. (1989), The relationship between slickenside surfaces in fine-grained quartz and the seismic cycle. *Journal of Structural Geology* 11(7), pp.879-893.
- Riedel, W. (1929), Zur mechanik geologischer Brucherscheinungen. *Zentralblatt für Mineralogie, Geologie und Palaeontologie* 1929B, pp.354-368.
- Scott, D.R., D.A. Lockner, J.D. Byerlee et al. (1994), Triaxial testing of Lopez Fault gouge at 150 MPa mean effective stress. *Pure and Applied Geophysics PAGEOPH* 142(3-4), pp.749-775.
- Scott, D.R., C.J. Marone & C.G. Sammis. (1994), The apparent friction of granular fault gouge in sheared layers. *Journal of Geophysical Research* 99(B4), pp.7231-7246.
- Stock, P. (1992), A strain model for antithetic fabric rotation in shear band structures. *Journal of Structural Geology* 14(10), pp.1267-1275.
- Taylor, G.I. (1938), Plastic strain in metals. *Journal of the Institute of Metals (U.K.)* 62, pp.307-324.
- Tchalenko, J.S. & N.N. Ambraseys. (1970), Structural analysis of the Dasht-e Bayaz (Iran) earthquake fractures. *Bulletin of the Geological Society of America* 81(1), pp.41-60.
- Turner, F.J. (1957), Lineation, symmetry, and internal movement in monoclinic tectonite fabrics. *Bulletin of the Geological Society of America* 68(1), pp.1-18.
- Twiss, R.J. & E.M. Moores. (2007), *Structural Geology* (2nd edition). W. H. Freeman and Company
- von Mises, R. (1928), Mechanik der plastischen Formänderung von Kristallen. *Zeitschrift für Angewandte Mathematik und Mechanik*(8), pp.161-184.